

# Hyper-Kamiokande Outer Detector Light Injector System Technical Note

Balint Bogdan\*, Sam Jenkins, Neil McCauley, Steve Boyd, Keith Jewkes,  
Menai Lamers James, Grace Hannaford, Ankush Mitra, Liz Kneale,  
Patrick Stowell

September 26, 2025

## 5 Contents

6	<b>0 Version history</b>	3
7	<b>1 Introduction</b>	4
8	<b>2 Light Injection System Overview and Requirements</b>	4
9	<b>3 OD PMT Saturation Study</b>	5
10	3.1 Diffuser Simulation . . . . .	6
11	3.2 Diffuser and OD Parameters . . . . .	7
12	3.3 Ssaturation Analysis . . . . .	8
13	3.4 Results . . . . .	9
14	<b>4 OD Collimator Studies</b>	11
15	4.1 Collimator Simulation . . . . .	11
16	4.2 Collimator Sensitivity Analysis . . . . .	12
17	4.3 Results . . . . .	12
18	<b>5 Diffuser Design</b>	13
19	5.1 ID Diffuser Hemisphere Design . . . . .	13
20	5.1.1 Inner Detector Diffuser Design . . . . .	13
21	5.1.2 Diffuser Profile Measurement System . . . . .	15
22	5.1.3 Diffuser Power Measurement System . . . . .	16
23	5.2 OD Diffuser Design . . . . .	17
24	<b>6 OD Diffuser Mounting System and Installation</b>	18
25	<b>7 Pulser Board</b>	19
26	7.1 Pulser Board Overview . . . . .	19
27	7.2 Physical Dimensions and Construction . . . . .	19
28	7.3 LED . . . . .	20
29	7.3.1 Overview . . . . .	20
30	7.3.2 Switching Circuit . . . . .	23

\*bbogdan@liverpool.ac.uk

31	7.3.3 Switch Selection . . . . .	23
32	7.3.4 Testing . . . . .	27
33	7.4 LVDS to TTL Converter . . . . .	28
34	7.5 Power Supplies . . . . .	29
35	7.6 Connector . . . . .	30
36	7.7 Fibre Coupler . . . . .	30
37	7.8 Photon Yield Tests . . . . .	31
38	7.9 Production . . . . .	31
39	7.10 Changes Expected from v0.9 to v1.0 . . . . .	34
40	7.10.1 LED and Switching Circuit . . . . .	34
41	7.10.2 LVDS-to-TTL Converter . . . . .	34
42	7.10.3 Power Supplies . . . . .	34
43	7.10.4 Connector . . . . .	34
44	7.10.5 Fibre Coupler . . . . .	34
45	<b>8 Server Rack and Cooling</b>	<b>35</b>
46	<b>9 LED Monitoring</b>	<b>35</b>
47	<b>10 Control System for LEDs</b>	<b>35</b>
48	<b>11 Crate Electronics</b>	<b>36</b>
49	11.1 Overview . . . . .	36
50	11.2 Blade . . . . .	37
51	11.3 Backplane . . . . .	38
52	11.4 Eurocard . . . . .	38
53	<b>12 Conclusions</b>	<b>39</b>

54 **0 Version history**

- 55     ● v0.99 - First release by Balint circulated to Liverpool group for internal review
- 56     ● v1 - [Sam]: Ported over to github for continued development, as we hit compilation  
57       time on overleaf. Initial pass through to fix wording and rewrite some sections. Also  
58       integrating Warwick TN on OD diffuser, and Liz's work on the OD saturation studies.  
59       Some reordering of structure to make it flow better.

60 **1 Introduction**

61 Hyper-Kamiokande is a large scale water Cherenkov detector with two main sections, an  
62 inner detector (ID) and an outer detector (OD). The OD volume of Hyper-K is a one meter  
63 wide annular ring on the circumference of the detector. This space is designed to tag charged  
64 particles, such as cosmic ray muons or particles from interactions in the surrounding rock,  
65 entering the detector. In addition, the OD volume will be used as working space for instal-  
66 lation activities. Once complete, it will be optically separated from the ID volume, and will  
67 be instrumented with 3,600 outward facing 8 cm photomultipliers tubes (PMTs). These will  
68 each surrounded by wavelength shifting (WLS) plates to increase photocoverage.

69 In order to achieve the precision measurements Hyper-K aims to make, precise calibration  
70 of the detector is required. For the OD, a light injection (LI) system will be employed,  
71 allowing for known quantities of light to be injected into the detector region. This will  
72 consist of 122 diffusers and 12 collimators. The diffuser system, which is described in this  
73 technical note, will be used to measure gain and timing properties of the OD PMTs, and  
74 will be powered by dedicated pulsed LED sources. The 12 OD collimators are identical to  
75 those uses in the ID system, and will be integrated into the ID laser system. Full details on  
76 that system, along with investigations of the fibre optics that will be employed for the OD  
77 system, can be found in [1].

78 **2 Light Injection System Overview and Requirements**

79 The OD diffuser system will be composed of 122 bare diffusers, installed on the outward facing  
80 side of the PMT support structure. The proposed layout for this is shown in Figure 1, though  
81 in actuality there will be minor differences from this regular arrangement due to restrictions  
from other systems. These are arranged such that they illuminate roughly an equal amount

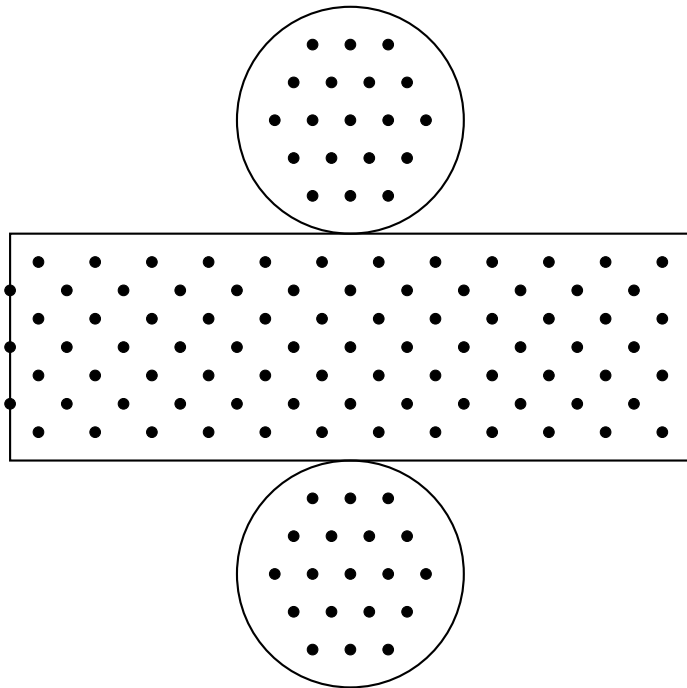


Figure 1: Injector location map for OD diffuser positions. Locations are approximate and dependent on PMT/WLS plate locations.

82  
83 of OD PMTs. One of the primary goals of the system is to inject enough light to saturate the

84 OD PMTs. This goal drives a large part of the photon output optimisation, and Monte Carlo  
85 (MC) studies to evaluate the amount of photons required to do this are shown in Section 3.  
86 The diffuser design is discussed in Section 5. These will each be illuminated by individual  
87 LED pulser boards with 365 nm LEDs. This will require at least 122 dedicated LED pulsers,  
88 and spares should be readily available for hot-swapping should a board encounter issues. Full  
89 details of the pulser board design are given in Section 7. The pulser boards will be powered  
90 and controlled by commercially-available Field Programmable Grid Array (FPGA) boards.  
91 The control system architecture for these consists of three primary components:

- 92 • **Blade:** Interfaces directly with the FPGA, distributing all differential signals into the  
93 crate system.
- 94 • **Backplane:** Routes differential signals to the pulser boards and provides the primary  
95 power distribution, accepting 12 V and  $\pm 5$  V inputs.
- 96 • **Eurocards:** Host the pulser boards, receive power and differential signals from the  
97 backplane, and incorporate the necessary circuitry for laser triggering.

98 Further details on the control system and individual electronics crate components are given  
99 in Sections 10 and 11 respectively.

100 Light will be transported between the pulsers and diffusers by a series of fibre optic  
101 cables; following the investigations in [1] the Thorlabs FP400URT [2] is targeted for this.  
102 Due to production limitations, it is not possible to keep all fibre path lengths the same.  
103 Instead there will be five different lengths: 50 m, 80 m, 106 m, 124 m and 168 m. The  
104 light output after signal attenuation and dispersion in these fibres should be as consistent  
105 as possible, which will require fine tuning given the different amounts of attenuation and  
106 dispersion which pulses will experience based on fibre length.

107 The initial design requirements for the system are to produce pulse widths out of the  
108 diffuser of no more than 10 ns, with a photon yield in the range 1–15 million photons per  
109 pulse (ppp). The 10 ns limit is driven by the timing resolution of the WLS plates. The  
110 wavelength of light used is also partially dictated by the WLS plates, which will not activate  
111 for light above 400 nm. The photon yield target here is more of a goal than a requirement,  
112 and saturation studies were performed using numbers motivated by system performance.  
113 These are summarised in Section 3.

114 The below paragraph should split up. The first half has been rewritten into the above  
115 paragraph, the second should be fleshed out for the photon yield test section. This will be  
116 removed once that is done.

117 Pulse width should ideally be between 1-10 ns and the photon count from 1-15 million  
118 photons, but higher limits are preferable. The lower limits are not possible to achieve, as the  
119 fibre dispersion will create a minimum pulse width, which is 4.5 ns at 180 metres, and if we  
120 try to achieve large light output it will compromise our lower light output, so we can only  
121 achieve around 100,000 photons per pulse at minimum. While these compromises are not  
122 ideal, the fibre selection limits our capabilities on hitting the required theoretical targets.

### 123 3 OD PMT Saturation Study

124 The light injection system in the OD will use collimated and diffuse light injection to calibrate  
125 the PMTs and to measure the optical properties (scattering and absorption) of water, as well  
126 as any degradation in Tyvek reflectivity over the course of operation.

127 Diffuse light sources will be used for in-situ calibration of the PMT charge response.  
128 Light will be injected at very low levels to measure the single-photoelectron charge response,  
129 and the requirement to achieve single-photoelectron coverage across all PMTs was used to

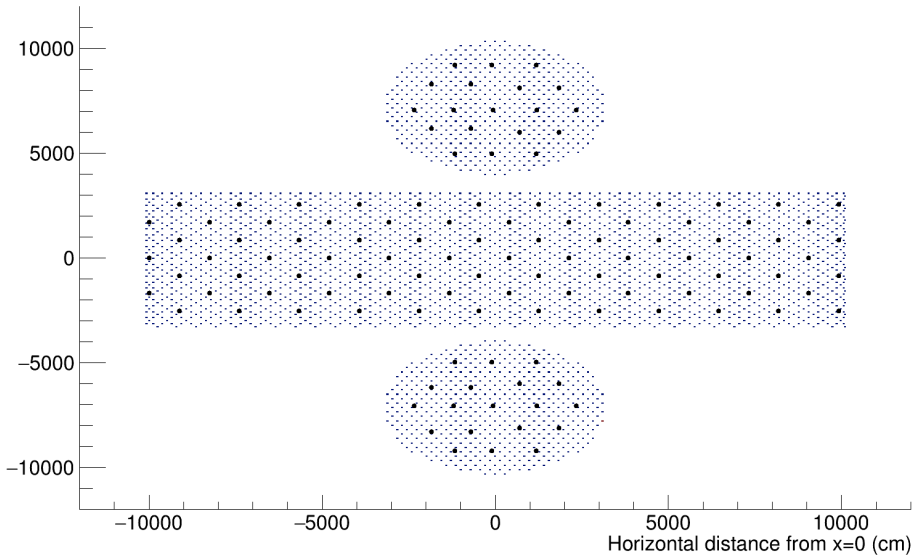


Figure 2: Positions of the OD PMTs and diffuser positions used in the calibration simulations. Note that the positions of PMTs in the top and bottom rows of the barrel have changed in the design, and as such the results presented in this tech note reflect these changes. This differs from the most recent version of WCSim (1.12.26) [4] that has been used as a basis for the simulation, and the changes are reflected in pull request #525.

130 determine the number of light injectors required for the light injection calibration system, as  
 131 reported in the Outer Detector Technical Report [3]. In order to calibrate the PMTs across  
 132 their entire range, the light injection system must also be capable of illuminating PMTs to  
 133 saturation, to understand the change in their response as they approach saturation.

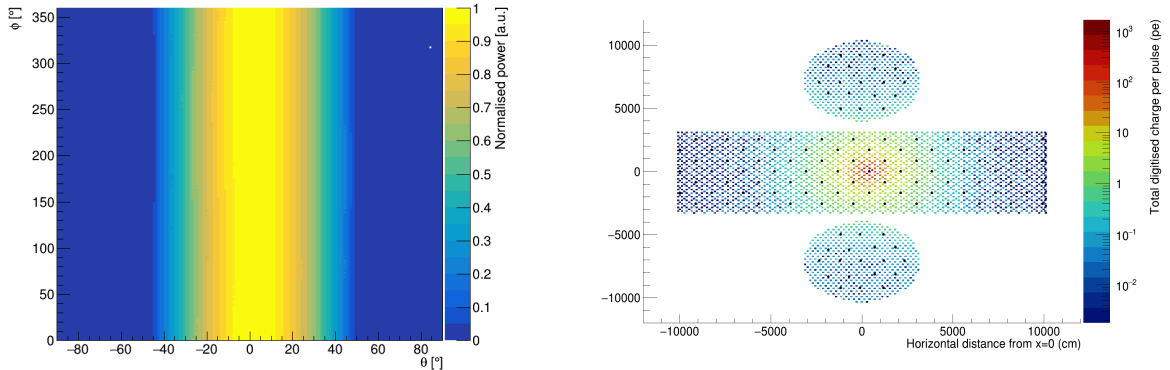
134 This section describes the use of diffuse light injection to evaluate the suitability of light  
 135 sources for in-situ measurements of the PMT saturation response. Section 3.1 describes the  
 136 diffuser simulation, Section 3.2 gives details of the OD geometry and diffuser parameters  
 137 used, and Sections 3.3 and 3.4 describe the scope, analysis and results of the saturation  
 138 study.

### 139 3.1 Diffuser Simulation

140 The planned light injection calibration system will include 122 diffusers, as determined by  
 141 maximising the single-photoelectron coverage of all of the OD PMTs [3]. The division of dif-  
 142 fusers between the endcaps and barrels, and their positions in terms of the overall geometry,  
 143 has been altered since [3], following an update of the design and geometry in the simulation.  
 144 Figure 2 shows the updated diffuse light injector (LI) locations with respect to OD PMT  
 145 positions. The diffusers have been positioned as close to equidistant as possible from the  
 146 surrounding PMTs, next to a strut in an empty cell.

147 A new LI generator has been written within the framework of WCSim [4]. This allows  
 148 the user to define the characteristics of the LI within a data file input to the simulation. The  
 149 following characteristics can be defined:

- 150 • Global position within the detector geometry,
- 151 • Direction of the LI axis,
- 152 • Wavelength of the optical photons



(a) ID diffuser profile measured in water, used for the diffuser simulations described in this technical report. A measured profile for each diffuser will be stored in the database for OD calibration.

(b) Charge in photoelectrons on each PMT produced when the profile in (a) is used to simulate optical photons from a diffuser pointing outwards in the barrel OD. The size of the PMT + WLS plates has been increased only in the plot for improved visualisation.

Figure 3: Diffuser profile measured in water, and the resulting charge map from this profile.

- 153 • Pulse width
- 154 • Photons per pulse
- 155 • LI profile in the form of arrays of  $\theta$ ,  $\phi$  and measured light intensity, where  $\theta$  is the  
156 angle made with the axis of the LI and  $\phi$  is the rotation around the axis.

The LI profile opening angle and intensity can reflect either a flat angular distribution of photons within the desired angular range of the light injector (-opening angle, +opening angle), or can be drawn from the measured profile for that injector, in which case the LI generator accurately models the variation across the profile, and in particular the drop-off in the frequency of photons towards the edge of the LI profile. For each pulse, the generator samples the specified number of photons per pulse, each with an energy calculated from the wavelength set in a database currently stored within WCSim, and a time sampled from a Gaussian distribution around the mean, with a variance equal to the pulse width specified in the database. Each photon is also assigned a global direction, which is sampled with a distribution corresponding to the LI profile.

The profile of each diffuser will be measured and stored in the database as a function of the diffuser identifier number in the final simulation. For the purposes of the diffuser simulations presented in this tech note, a single profile taken from the measurement of a diffuser profile in water has been used. This diffuser profile corresponds to an opening angle of around 40°. Since the OD diffuser profiles have not yet been measured in water, an ID diffuser profile has been used to approximate a realistic OD diffuser profile. Although the design of the OD diffusers has been modified from the ID diffuser design in order to increase the diffuser efficiency, the design has been shown to maintain the desired profile and as such the ID diffuser profile is expected to be a reasonable approximation. The diffuser profile used, and the resulting charge map from a diffuser in the barrel is shown in Figure 3.

### 177 3.2 Diffuser and OD Parameters

178 The characteristics of diffusers simulated in the saturation study are summarised in Table I.  
179 The number of photons per pulse used in the simulation was based on measurements made

180 from the LED pulser setup, using a chain of fibre optic cables equating to 181 m in length.  
 181 The simulations described here use a maximum photon yield from the fibre optic chain of  
 182  $11 \times 10^6$  photons per pulse. This was modified to account for an assumed diffuser efficiency  
 183 of 50%. As such, the simulated number of photons per pulse is  $5.5 \times 10^6$ .

Parameter	Assumed value
Photons per pulse	$11 \times 10^6$
Wavelength	365 nm
Pulse width	10 ns
Diffuser efficiency	50%

Table I: The LI configuration used in the diffuser simulations for the saturation study presented in Section 3.3.

184 The OD geometry parameters that have been used in the simulations for the saturation  
 185 study are shown in Table II.

Parameter	Assumed value
PMT radius	8 cm
PMT dark rate	0.4 kHz
OD lateral water depth	1 m
OD height water depth	2 m
OD dead space	60 cm
Tyvek sheet thickness	1 mm
WLS plate thickness	6 mm
WLS plate length	30 cm

Table II: The OD configuration used for the saturation study presented in Section 3.3 using WCSim version 1.12.26.

### 186 3.3 Saturation Analysis

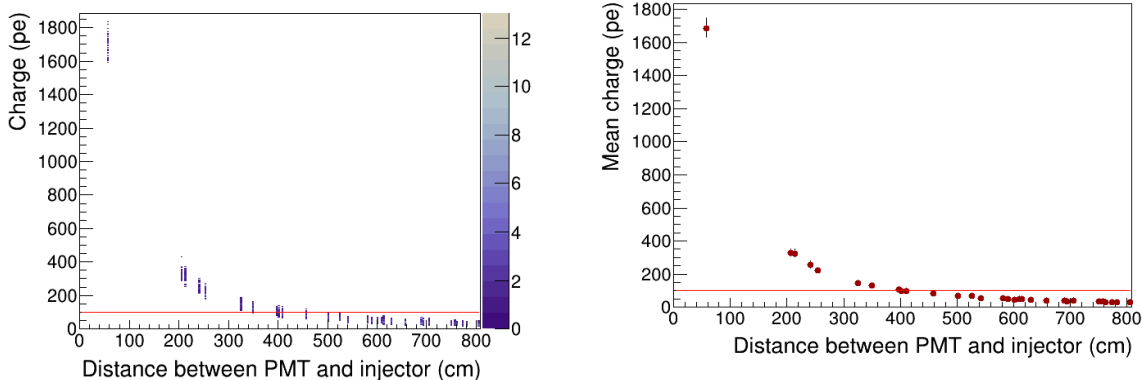
187 The limit of the PMT range is governed by the electronics response, which is expected to  
 188 fully saturate at around 100 photoelectrons (pe) in a 16 ns time window. The simulation  
 189 of the PMT charge response in WCSim does not currently handle the saturation, but it is  
 190 expected that the linearity of the charge response will break down between 80 pe and 100 pe.  
 191 Saturation measurements aim to measure the PMTs over the full range of this breakdown  
 192 in linearity. The saturation level for the purposes of this study has been taken to be 100 pe  
 193 in 16 ns, but the analysis has been designed to take into account the need to measure across  
 194 the entirety of this range.

195 The saturation of OD PMTs has been evaluated in the top endcap, barrel and bottom  
 196 endcap. The diffuser simulations are intensive, requiring millions of tracked photons to  
 197 simulate a single flash. As such, only two diffusers in each of the top endcap, barrel and  
 198 bottom endcap have been simulated for this current study.

199 Two values have been used as figures of merit to determine the PMT saturation coverage:

- 200 • Mean saturation distance - the distance from the nearest diffuser at which the mean  
 201 charge per PMT is greater than saturation level.
- 202 • Saturation limit - the greatest distance from the nearest diffuser at which the charge  
 203 on any PMT reaches the saturation level.

For each configuration, the charge per PMT was plotted as a function of the distance from the nearest diffuser, to give the saturation limit (Figure 4a). The mean saturation distance was then found by taking the mean of the same plot (Figure 4b). The plot showing the saturation limit is particularly useful in understanding the range of distances over which it is possible to see the expected range of breakdown of linearity.



(a) Plot of the charge per PMT as a function of the distance from the nearest diffuser. The saturation limit is the greatest distance at which saturation is achieved i.e. 5.0 m in this case.

(b) Plot of the mean charge per PMT found by taking the mean of the left-hand plot. The mean saturation distance is the greatest distance at which the mean charge per PMT is greater than the saturation level i.e. 4.0 m.

Figure 4: Sample plots showing the mean saturation distance and saturation limit used as figures of merit for the saturation study. The red, horizontal lines mark the assumed saturation level of 100 pe.

Since only six diffuser locations have been simulated, the percentage of PMTs within the mean saturation distance and saturation limit is calculated assuming symmetry both of the detector and of the diffuser positions with respect to the PMTs. However, for practical reasons, the diffusers have to be positioned off-centre in the empty cells between PMTs, next to the struts on the PMT support structure. As such, a full simulation of all diffusers should be performed in future, once the OD geometry and LI specifications have been finalised, for an accurate evaluation of the percentage saturation across the whole detector.

### 3.4 Results

The mean saturation distance and saturation limit were evaluated for two OD diffuser locations in each of the top endcap, barrel and bottom endcap. These are shown in Table III, along with the percentage of PMTs within the mean saturation distance and saturation limit. Table IV shows the mean charge at the calculated saturation distance and the mean charge at the saturation limit at the six diffuser positions.

Figure 5 shows the PMT charge map for the Barrel 1 diffuser, with the saturation distance and saturation limits marked around the barrel PMTs.

Due to the differing geometry the mean saturation distance in the barrel (4.0 m) is slightly higher than in the endcaps (e.g. 3.6 m), and the percentage of PMTs within the mean saturation distance in the barrel is higher at 31% than in the endcaps (22-27%). Similarly, the percentage of PMTs within the saturation limit in the barrel is higher than in the endcaps, with the exception of the bottom endcap 2 diffuser, with 66% of PMTs within the saturation limit of 6.1 m. It should be noted that changes to the OD geometry, including the addition of PMTs in the endcaps, are possible, and have not been taken into account in this simulation.

OD location	Mean saturation distance	% PMTs within saturation distance	Saturation limit	% PMTs within saturation limit
Barrel 1	4.0 m	31%	5.0 m	50%
Barrel 2	4.0 m	31%	5.0 m	50%
Top endcap 1	3.7 m	27%	3.9 m	30%
Top endcap 2	3.6 m	24%	4.3 m	37%
Bottom endcap 1	3.6 m	24%	4.3 m	37%
Bottom endcap 2	3.5 m	22%	6.1 m	66%

Table III: Results for PMT saturation using the diffuser configuration detailed in Table I.

OD location	Diffuser position (cm)	Mean charge (pe) at sat. distance	Mean charge (pe) at sat. limit $\pm 2\sigma$
Barrel 1	(395.65,-3281.50,8.75)	108	$68 \pm 12$
Barrel 2	(3281.50,395.65,1705.55)	105	$67 \pm 11$
Top endcap 1	(-70.7,-97.3,3350.82)	106	$96 \pm 14$
Top endcap 2	(-707,-968.2,3350.82)	108	$77 \pm 13$
Bottom endcap 1	(-707,-968.2,-3350.82)	108	$77 \pm 14$
Bottom endcap 2	(707,-1157.8,-3350.82)	114	$42 \pm 11$

Table IV: Results for PMT saturation using the diffuser configuration detailed in Table I.

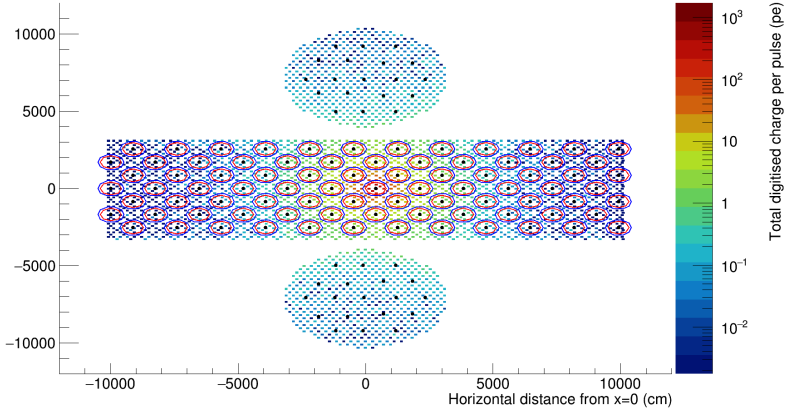


Figure 5: Charge in pe on each PMT as a result of illumination with the Barrel 1 diffuser. The mean saturation distance and saturation limit around each PMT in the barrel are marked in red (smaller circles) and blue (larger circles) respectively.

The diffuser position with respect to the surrounding PMTs has an observable effect on the saturation levels achieved. Where the diffuser positions with respect to surrounding PMTs are equivalent, as in the case of the two barrel diffusers, as well as the Bottom Endcap 1 and Top Endcap 2 diffusers, saturation levels are largely the same. However, the positions of the Top Endcap 1 and Bottom Endcap 2 diffuser each differ from all other diffusers simulated, resulting in different saturation distances and saturation limits. Again, a full simulation of all diffuser positions should be carried out to fully evaluate achievable saturation across the whole detector, once all parameters and geometries have been finalised.

240 **4 OD Collimator Studies**

241 Collimated light sources will be used to make measurements of scattering and absorption in  
242 water, and Tyvek reflectivity. These will be used to calibrate for changes in the detector  
243 properties over time. This will require untangling the effect of each of the properties in order  
244 to discriminate changes in each of the properties. The first step is to evaluate the sensitivity  
245 of collimators to changes in each of the properties separately.

246 This section presents the collimator sensitivity studies which were carried out prior to  
247 updates to the OD geometry and more recent updates to the light-injector simulation. Sec-  
248 tion 4.1 describes the positioning of collimators, and the simulation method. The analysis of  
249 sensitivity to water properties and Tyvek reflectivity are presented in Section 4.2, and the  
250 results are presented in Section 4.3.

251 **4.1 Collimator Simulation**

252 The collimated light sources were simulated using the LI simulation described in Section 3.1.  
253 For this collimator study, a flat profile with an opening angle of  $2^\circ$  was taken as the baseline,  
254 and the OD configuration described in Table II in Section 3.2 was used. Figure 6 shows the  
255 charge map produced by the  $2^\circ$  collimator source in the top endcap.

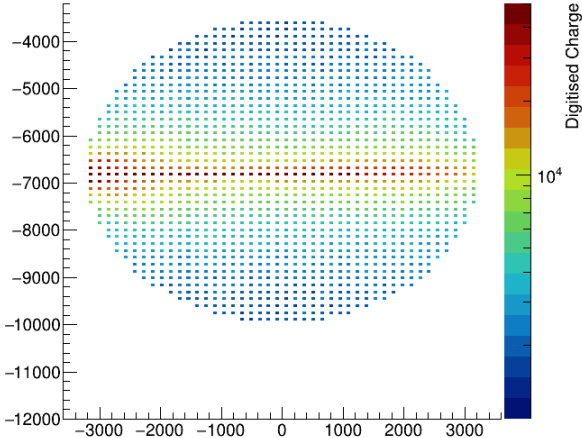


Figure 6: Distribution of charge collected in end cap PMTs for a collimated beam of light injected from the right hand side, travelling across the diameter of the OD to the left hand side.

256 The sensitivity of each of the collimators to changes in absorption, Rayleigh scattering  
257 and Tyvek reflectivity was evaluated by varying each property one at a time, scanning over  
258 values up to 30% either side of the nominal value for absorption and scattering, and 30% lower  
259 than the expected value for Tyvek reflectivity. Nominal values have been extrapolated  
260 from Super-Kamiokande measured values in the case of scattering and absorption, and from  
261 the expected value in the case of the Tyvek reflectivity. These values and the range of the  
262 scans over each property are shown in Figure 7.

263 Variable steps were chosen for the scan over the range for each property to allow suf-  
264 ficiently detailed evaluation of the sensitivity to changes in each property. For absorption  
265 and scattering, the parameters are varied in steps of 1% between  $\pm 5\%$ , where finer binning  
266 is required to see the small effects at these variations. From 5% to 30% either side of the  
267 nominal, the parameters were varied in 5% steps. For Tyvek reflectivity, the parameter is

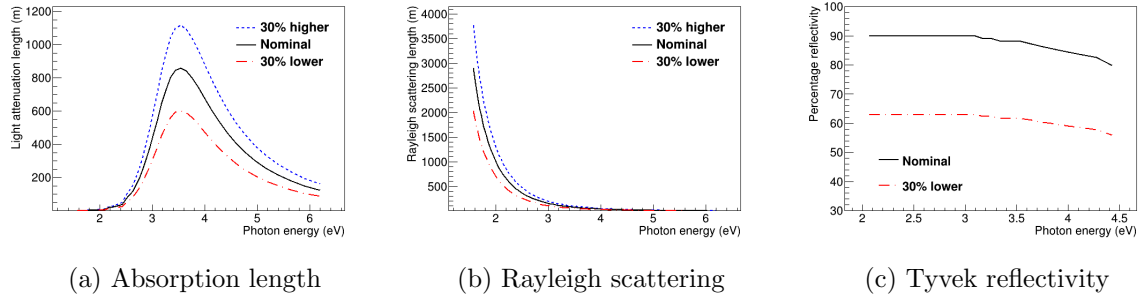


Figure 7: Nominal (black, solid), maximum (blue, dashed) and minimum (red, dot-dashed) values for the scans over absorption length and Rayleigh scattering, and nominal (black, solid) and minimum (red, dot-dashed) values for the scans over Tyvek reflectivity.

reduced by up to 30% either side of the nominal, in 0.5% steps up to  $\pm 5\%$ , 1% steps between  $\pm 5\%$  and  $\pm 10\%$  and in 5% steps above that.

The scans over the variation in parameters require at least 21 individual simulations per property, and each simulation requires  $\mathcal{O}(100M)$  photons to produce sufficient statistics. In addition, the OD geometry remains in flux. As such, although the OD light injection system will include 12 OD collimators, a single collimator in each of the OD top endcap, barrel and bottom endcap was simulated for the purposes of these studies.

## 4.2 Collimator Sensitivity Analysis

To evaluate the sensitivity of the collimator to each of the parameters, the distribution of charged collected in the PMTs as a function of the distance from the light injector was compared over the scan ranges detailed in Section 4.1. These were compared using a Pearson's chi-squared test:

$$\chi^2 = \sum_{s=0}^S \frac{(O_s - E_s)^2}{E_s}, \quad (1)$$

where the expected value  $E_s$  is the charge on the PMTs at distance  $s$  for the nominal parameter value, and the observed value  $O_s$  is the charge on the PMTs at distance  $s$  for the varied parameter value. In this way, the distribution of chi-squared values as a function of the percentage change in parameter value indicates the sensitivity of the collimator to the changes in each of the properties. For the baseline analysis, only PMTs located in the same part of the detector were included in the chi-square calculation.

Errors on the chi-squared statistic were calculated by splitting the sample into 10 sub-samples, calculating the Pearson's chi-squared test statistic for each sub-sample and then calculating a relative standard deviation from the variance between the sub-samples.

## 4.3 Results

Figure 8 shows the chi-squared/ndof values over the scan ranges for each of the properties investigated for a  $2^\circ$  collimator located at the bottom of the OD and pointing upwards in the OD barrel. The collimator is most sensitive to changes in reflectivity, and least sensitive to changes in absorption.

The location of the collimator, in terms of distance from the front face of the PMTs, can affect the sensitivity to changes in the parameters. ??

The collimators have been designed to be tunable to different open angles. A comparison of the results for a  $2^\circ$  and  $1.35^\circ$  collimator in the same position in the barrel is shown in Figure 9. With a straight comparison of the Pearson's chi-squared test statistic for the

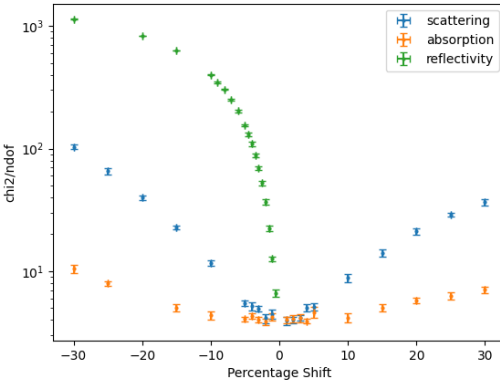


Figure 8: Change in chi-squared statistic with variation in absorption (orange), Rayleigh scattering (blue) and Tyvek reflectivity (green) up to 30% from the nominal value.

295 two collimators, there was no obvious change in the sensitivity to changes in any of the  
296 parameters.

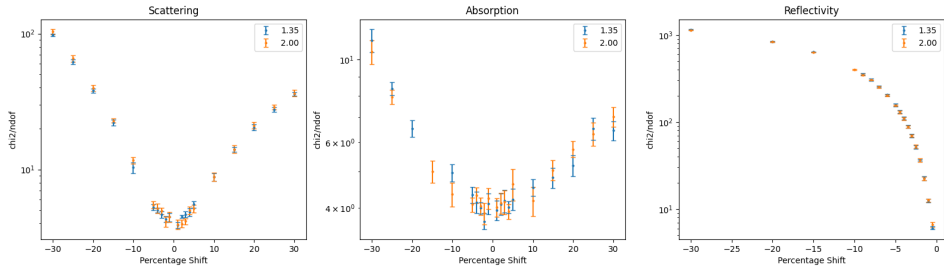


Figure 9: Change in chi-squared statistic with variation in Rayleigh scattering (left), absorption (centre) and Tyvek reflectivity (right) up to 30% from the nominal value for a 2° collimator (orange) and 1.35° collimator (blue).

## 297 5 Diffuser Design

### 298 5.1 ID Diffuser Hemisphere Design

#### 299 5.1.1 Inner Detector Diffuser Design

300 The diffusers used to scatter input laser light in the inner detector volume are 2.54 cm  
301 half-spheres fabricated from PTFE. This is used as it

- 302 • is unaffected by immersion in water
- 303 • acts as a excellent diffuser
- 304 • is a good transmitter of UV light
- 305 • is easy to machine and clean

306 A mechanical drawing of the inner detector diffuser hemispheres is shown in Figure 10

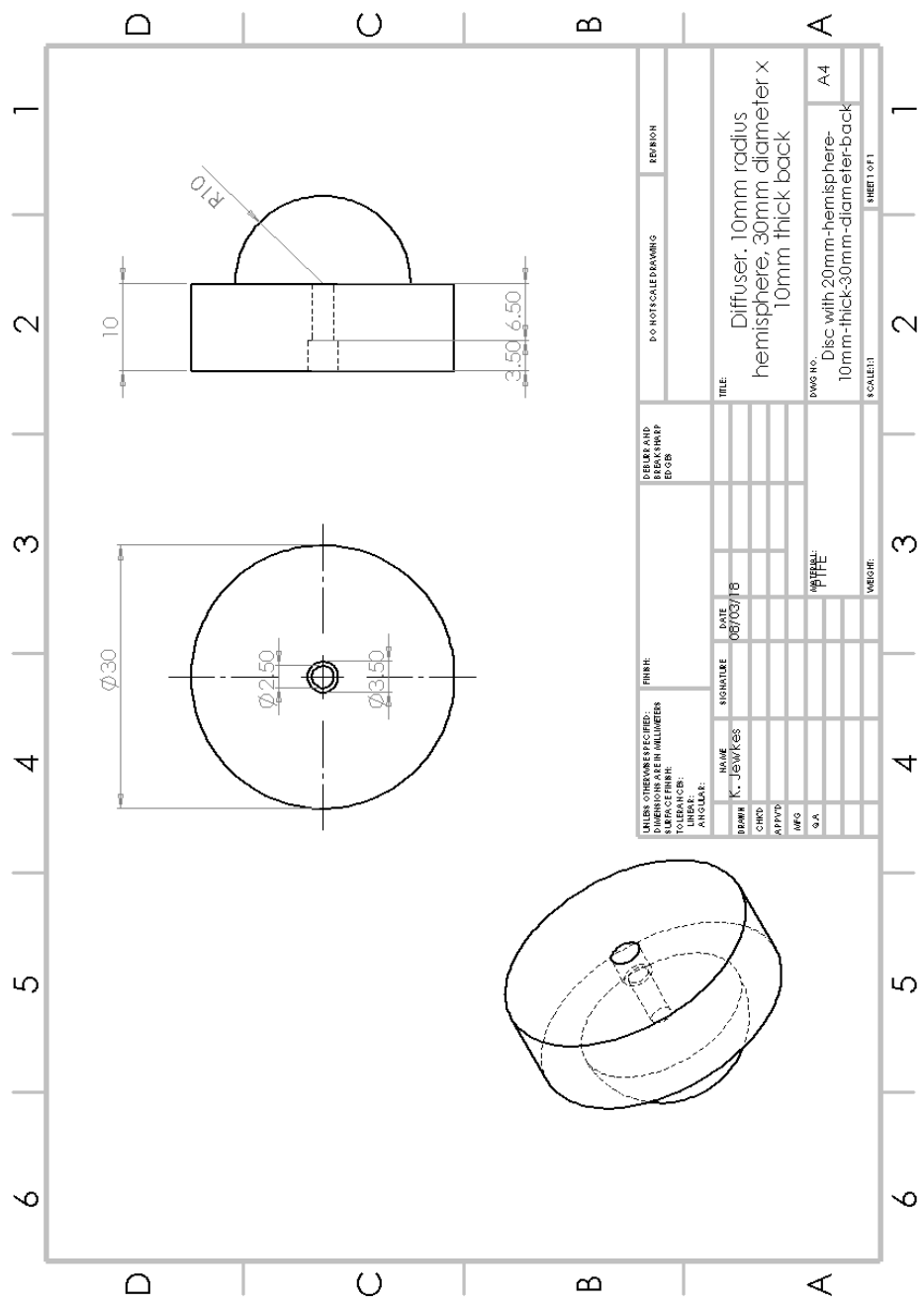


Figure 10: Bare Diffuser Mechanical Drawing

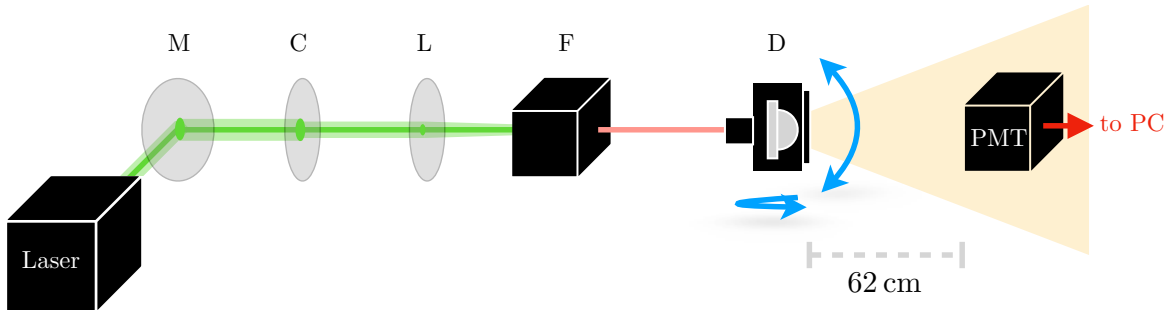


Figure 11: Setup for diffuser scans: light from the laser is directed via a mirror (M), a circulator (C), and a lens (L) to the fibre launch stage (F). From there, the light goes via an optical fibre to the diffuser (D) on the rotation stage.

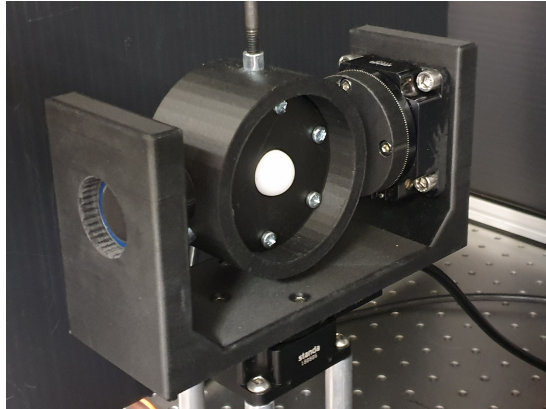


Figure 12: Rotation stage with bare diffuser hemisphere mounted using a 3D-printed frame.

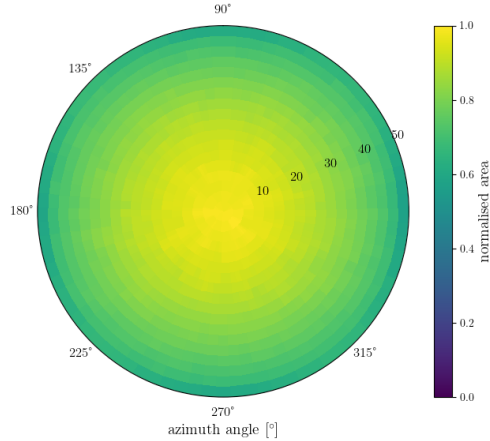
### 307 5.1.2 Diffuser Profile Measurement System

308 A scanning system was built to measure the output characteristics of diffuser hemispheres.  
 309 Enclosed in a dark box, the diffuser is mounted onto two rotary stages which gives the freedom  
 310 to rotate the diffuser around the nominal axis linking the diffuser with the photosensor. This  
 311 scanner only takes scans in an air medium, and the setup is illustrated in Figure 11.

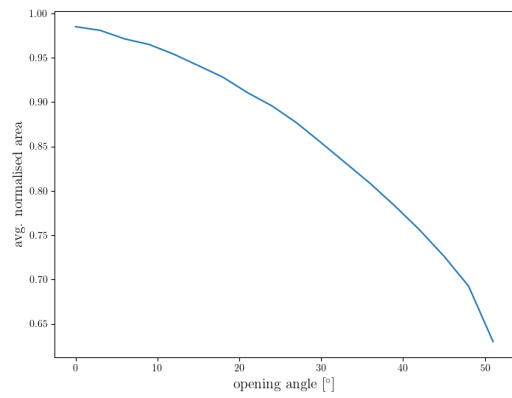
312 A laser powered from a wall plug is used to illuminate the diffuser with light at a wave-  
 313 length of 450 nm. It is triggered by a function generator with 1000 triggers per burst at a  
 314 frequency of 2 kHz. The open beam is directed via a mirror, a circulator, and a lens to the  
 315 fibre launch stage, and then via an optical fibre towards the diffuser. The diffuser enclosure is  
 316 fixed with three screws on the double-rotation stage. Measurements of bare diffuser profiles,  
 317 i.e. without enclosure, are conducted with the bare fibre end positioned in the centre of the  
 318 rotation stage using a 3D printed frame. The bare fibre end is kept in place due to friction  
 319 on the connection point with the diffuser hemisphere. A photograph of the rotation stage  
 320 with a bare diffuser hemisphere is shown in Figure 12.

321 A PMT measures the diffuser spectrum at a fixed position, with 62 cm distance to the  
 322 diffuser enclosure and a 3 mm pinhole aperture, restricting the solid angle viewed by the PMT  
 323 to  $2 \cdot 10^{-5}$  sr. For comparison, a single 50 cm PMT in the HK far detector receives light from  
 324 a point source at the other side of the tank over a solid angle of approximately  $2.2 \cdot 10^{-4}$  sr.  
 325 The PMT signal is digitised at a sampling rate of 2500 MHz over 1000 cycles, allowing to  
 326 resolve the shape of each single signal waveform. The light yield at each coordinate is then  
 327 obtained as the average waveform area across all digitised signals.

328 The diffuser profile measurement system is discussed in detail in [5].



(a) 2D polar histogram of bare ID hemisphere



(b) Radial profile of bare ID hemisphere

Figure 13: Profile scan of a standard bare ID diffuser hemisphere

### 329 5.1.3 Diffuser Power Measurement System

330 In addition to the profile measurement functionality, the integrated power output from the  
 331 diffuser was measured using an integrating sphere from Ophir. This sphere provides an  
 332 unbiased measurement of the total light output power of any light source, regardless of the  
 333 shape of the emission profile. A bespoke diffuser holder suitable for connection to one of the  
 334 integrating sphere ports was 3D-printed, as was a holder for the optical fibre from the laser  
 335 source.

336 A bare PTFE hemisphere was mounted into this holder and connected into the integrating  
 337 sphere port. The bare end is inserted into the connection point in the same manner as for  
 338 a bare profile scan. Tape was used to prevent light leaking out of the back  
 339 of the hemisphere during the measurement, which also helped to keep the fibre in place.  
 340 The hemisphere was then illuminated with light from the same laser, this time running on  
 341 a continuous rather than burst setting. On the continuous setting light is supplied in a  
 342 sinusoidal manner at a frequency of 1 kHz. Power measurements were taken once per second  
 343 for a period of ten seconds to account for small fluctuations in laser intensity, the mean of  
 344 which served as the final power measurement for that hemisphere.

345 In order to calculate a power ratio, a measurement of power for the bare fibre also needed  
 346 to be obtained. This was done in a similar manner to a power measurement for a hemisphere,  
 347 using the same laser and data acquisition settings. To make the comparison between fibre and  
 348 hemisphere measurement as accurate as possible, a special hemisphere was created with the  
 349 fibre connection point extended into a hole that runs through the length of the hemisphere.  
 350 The bare fibre can then be inserted all the way through until it pokes out of the front,  
 351 allowing a power measurement for the bare fibre to be taken with the conditions inside the  
 352 integrating sphere as close as possible to hemisphere measurements. The ratio of hemisphere  
 353 power to fibre power can then be taken to determine the amount of light lost.

354 A table of systematics for the power ratio measurement is shown in Table V. Rotation  
 355 refers to changing the orientation at which the diffuser is placed into the holder, and dif-  
 356 fuser re-insertion refers to removing the diffuser from the holder and replacing it. Fibre  
 357 re-insertions refers to disconnecting and re-connecting the fibre into the diffuser, while bare  
 358 fibre refers to dis- and re-connecting the fibre when taking bare fibre measurements. This  
 359 results in a total systematic of 5.3% for a diffuser measurement and 1.8% for a fibre mea-  
 360 surement, and therefore an uncertainty of 5.6% in a power ratio measurement.

Systematic	Std. dev. (%)
Rotation	1.4
Diffuser re-insertion	1.0
Fibre re-insertion	5.0
Bare fibre re-insertion	1.8

Table V: Integrating sphere systematics for the power ratio measurement.



Figure 14: A prototype of the OD diffuser with a 2 mm top hat.

## 361 5.2 OD Diffuser Design

362 The original intention was to use the same diffuser hemisphere design for the OD diffusers  
 363 as will be used for the ID diffusers. However, the standard diffuser emits less than 20% of  
 364 the power delivered by an optical fibre. As there are a number of interfaces in the optical  
 365 pathway between the light source and the diffuser, and as the light source for the OD will  
 366 be LEDs, this was considered too low to be able to effectively saturate PMTs in the OD  
 367 space, which is one of the primary design requirements of the system. Neither the number of  
 368 interfaces in the optical chain, nor the light source can be changed easily, but it is possible  
 369 that an alternate design of the diffuser hemisphere could yield more light.

370 Light is lost to two mechanisms in the standard diffuser; absorption by the PTFE and  
 371 backscattering. Both loss mechanisms would be minimised if there were less PTFE in the  
 372 light path. The design for the OD diffuser section was modified to be the shape of a top  
 373 hat, as shown in Figure 14. The optimal depth was studied by taking profile and power  
 374 ratio measurements using the same diffuser, but at smaller and smaller depths; after each  
 375 measurement was completed, 2.0 mm was cut from the top-hat, and the measurements were  
 376 re-taken. This procedure was repeated until the top-hat was 2.0 mm high.

Top-hat depth (mm)	Power ratio (%)
10.0	19.2
8.0	32.4
6.0	31.5
4.0	42.1
2.0	55.2

Table VI: Power ratio measurements for each depth of the top-hat

377 Results of the power ratio measurements are shown in Table VI. As expected, power ratio  
 378 increases with decreasing top-hat depth, making the optimum depth 2.0 mm. The profile as

379 shown in Figure 15 confirms that the shape of the profile is still suitable.

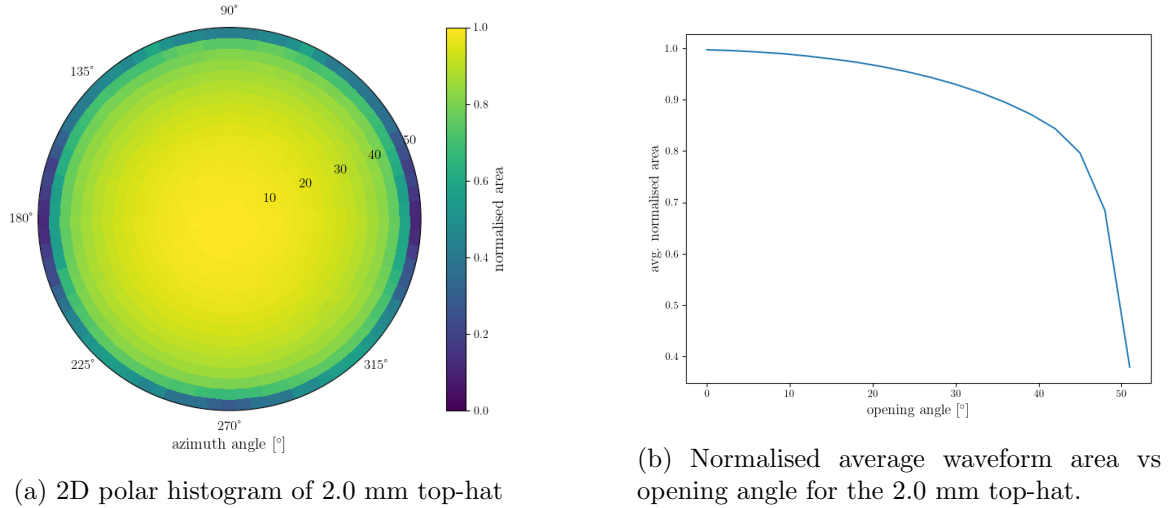


Figure 15: Profile scan of the 2.0 mm top-hat

380 Based on these studies, we propose to change the OD diffuser design from a hemisphere  
 381 to a top-hat with a 2.0 mm height above the base. The diffuser will still be fabricated from  
 382 PTFE, but this new design (i) emits more light at higher emission angles (ii) doubles the  
 383 amount of light that is emitted for a given LED power setting and (iii) is significantly easier  
 384 to fabricate in bulk.

## 385 6 OD Diffuser Mounting System and Installation

386 The OD space will be illuminated by a total of 122 OD diffusers, 19 on each of the top and  
 387 bottom caps, and 84 in the barrel. The barrel diffusers are distributed in 7 vertical layers  
 388 each consisting of 12 OD diffusers. Due to the numbers and cost, the mounting system must  
 389 be relatively small, easy to fabricate and easy to install. Installation will be carried out by  
 390 workers on the gondola in the OD space after the Tyvek has been installed and as the fibres  
 391 are being installed. The gondola worker will install the fibre in the OD diffuser, and fix the  
 392 mount to the HK frame, oriented into the OD space. Since this is being done on the gondola,  
 393 the mount needs to be small, easy to store, and straightforward to install.

394 Drawings for the OD diffuser prototype mount can be seen in Figure 16 and pictures  
 395 of the prototype can be seen in Figure 17. The mount is made from stainless steel and is  
 396 designed to hook over a horizontal frame bar, and screw in from the bottom. The PTFE



Figure 16: (left) Front view of the prototype of the OD diffuser mount and (right) rear view of the prototype of the OD diffuser mount.

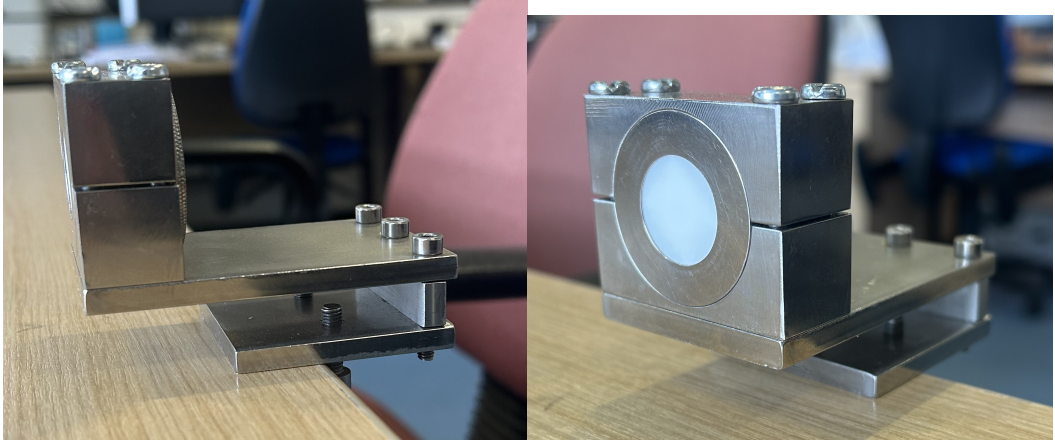


Figure 17: (left) Side view of the prototype holder and (right) front view of the prototype holder.

397 mount is approximately 5 cm on a side. The fibre will be installed from the back and is held  
 398 in place by a T-shaped component that is screwed down by the gondola worker. An image of  
 399 the prototype housing installed on the PMT support structure mockup next to a mechanical  
 400 OD PMT and WLS plate is given in Figure 18.

## 401 7 Pulser Board

### 402 7.1 Pulser Board Overview

403 The pulser board was designed to be a more efficient and compact version compared to  
 404 Super-Kamiokande UK Light Injection system, improving on efficiency, functionality, and  
 405 light output. The pulser board is a rather simple board designed for low cost production.  
 406 This section explains each circuit, component selection and design decision. Minor changes  
 407 are expected from the current design, mostly centred on removing prototyping circuitry.  
 408 More details on the expected changes are given in Section 7.10.

### 409 7.2 Physical Dimensions and Construction

410 The dimensions of the Printed Circuit Board (PCB) were selected to be as compact as practi-  
 411 cible, while still providing sufficient area for the secure mounting of a fibre coupler and for  
 412 the components. The final board size is 50 mm × 30 mm. This configuration permits elec-  
 413 trically noisy components, such as switching power supplies and the Low Voltage Differential  
 414 Signal to Transistor Transistor Logic (LVDS-to-TTL) converter to be positioned at a max-  
 415 imum distance from the switching circuitry, thereby minimising potential electromagnetic  
 416 interference.

417 Although it is technically feasible to further reduce the board size, preliminary design  
 418 studies and practical build indicated no substantial benefit in doing so. The board density  
 419 cannot be significantly increased inside the crate due to FPGA LVDS count and Eurocard  
 420 dimension, and cost analyses revealed negligible differences associated with a smaller PCB  
 421 footprint. Furthermore, the chosen dimensions provide an adequate area for the fibre coupler  
 422 and the necessary mounting holes to affix the pulser board onto the Eurocard, thereby  
 423 ensuring reliable optical alignment and mechanical stability. The PCB is fabricated as a four-  
 424 layer FR4 [6] board with a thickness of 0.8 mm, in accordance with the standard construction



Figure 18: OD diffuser housing installed at the RAL mockup frame, next to an OD PMT and WLS plate.

425 offered by PCB Train/Newbury Electronics<sup>1</sup>, see Figure 19. Refer to Figure 20 for the 3D  
 426 model of the pulser board. The Top Layer and Inner Top Layer are shown in Figure 21, and  
 427 the Inner Bottom Layer and Bottom Layer are likewise illustrated in Figure 22. A combined  
 428 view of all PCB layers is provided in Figure 23.

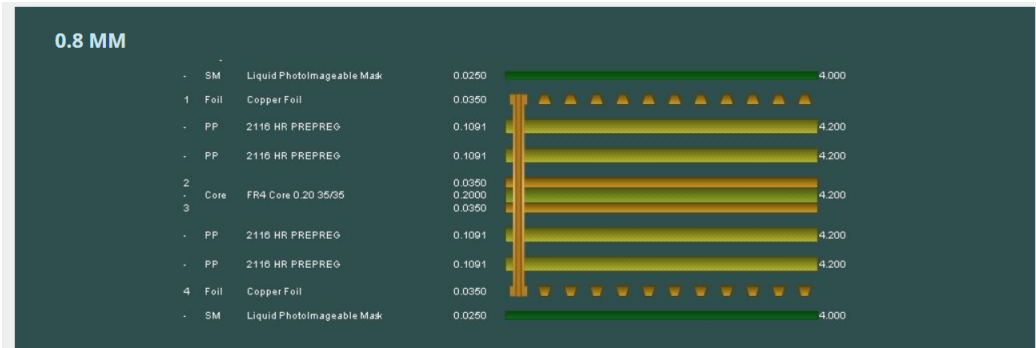


Figure 19: PCB Train's 4 Layer 0.8mm Layer Stack

### 429 7.3 LED

#### 430 7.3.1 Overview

431 The LEDs are the most crucial component in the system as the characteristics of these  
 432 primarily determine the light output, regardless of electronics. LEDs are usually not rated  
 433 for such high-speed applications, which meant LEDs had to be tested and validated in-house,

<sup>1</sup>These are trading names of the same manufacturer.

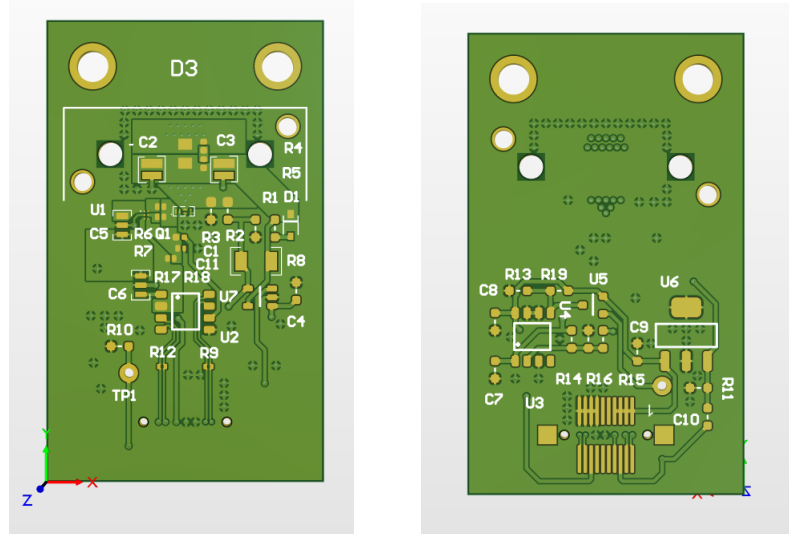


Figure 20: Pulser Board's 3D view Top and Bottom

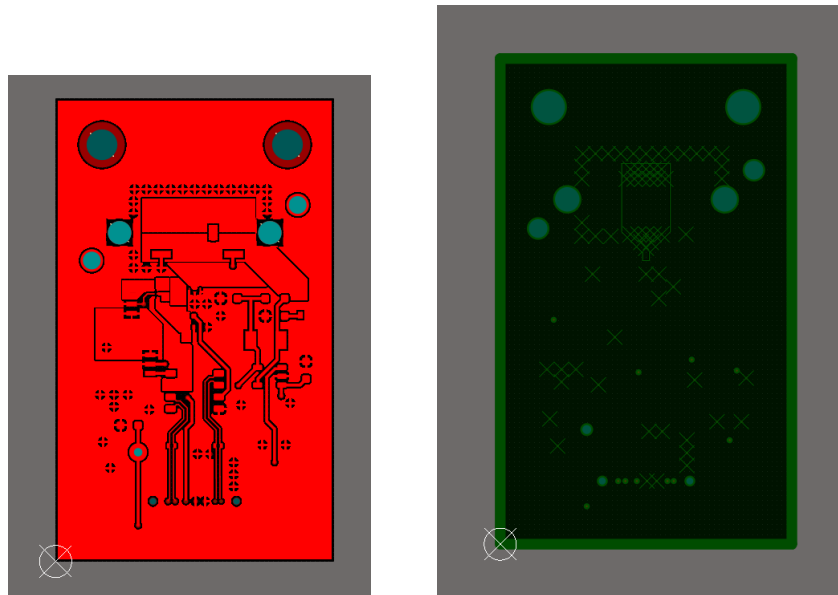


Figure 21: Pulser Board Top and Inner Top Layer

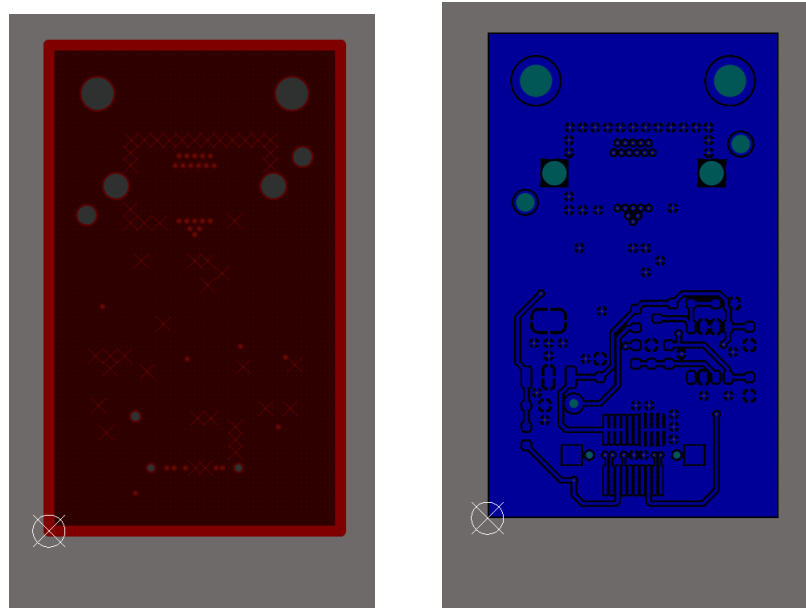


Figure 22: Pulser Board Inner Bottom and Bottom Layer

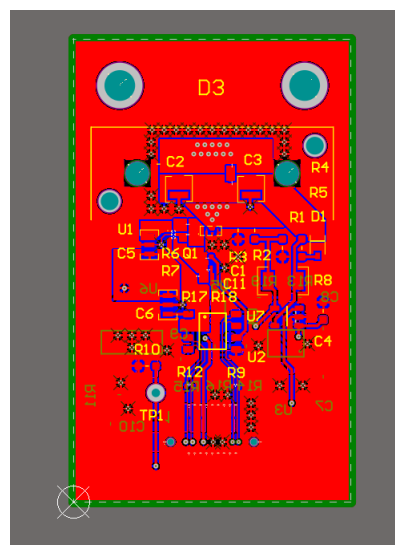


Figure 23: Pulser Board Layer Overview

434 as datasheets do not provide the required information. The specification required was a 1–  
435 10 ns clean single pulse, sub-400 nm wavelength, small surface mount package, narrow output  
436 beam so it can be coupled to a fibre with reduced losses and a good range of photon output.  
437 Several LED packages were purchased from Kingbright and LC-LED, and their performance  
438 tested. The results of these tests are given in Section 7.3.4.

### 439 7.3.2 Switching Circuit

The redesign process provided a valuable opportunity to evaluate a revised layout and new components for the switching circuit. Several enhancements have since been implemented in the revised switching circuit. Most importantly, the switching side of the layout has been rerouted. In contrast to the previous configuration, where current would flow through the limiting resistor regardless of the LED state, the updated design only allows current flow when the LED is active (refer to Figure 24). This modification reduces both thermal dissipation and the overall power consumption of the system. To modulate light intensity, a variable power supply is now employed to adjust the voltage supplied to the LED. This method has proven highly effective. Tests were conducted at various voltage levels using the full 181 m length of optical fibre—the maximum expected in Hyper-K at the time of testing—and the resulting photon output ranged from approximately  $1 \times 10^5$  to  $2 \times 10^7$  photons per pulse. Refined testing results are shown in Section 7.3.4. Further discussion regarding the implementation and performance of the variable voltage supply is provided in Section 7.5.

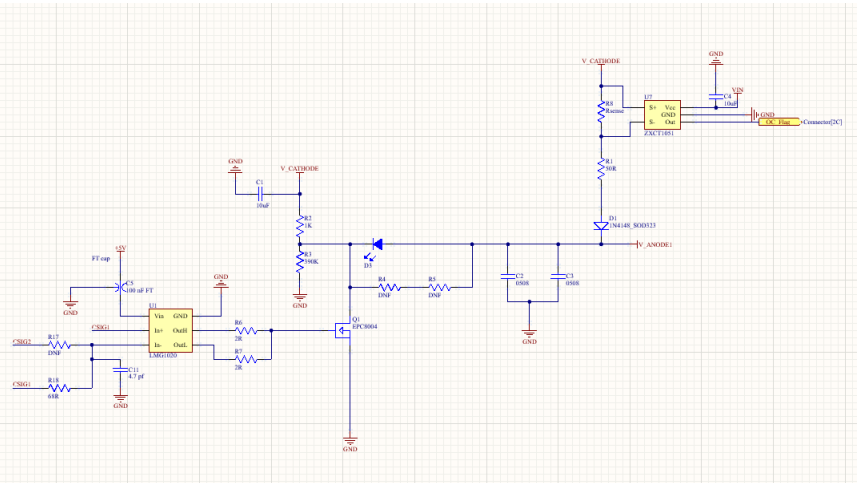


Figure 24: Switching Circuit Layout with LMG1020 and over current IC, R4 is 6.8 nH inductor and R5 is 3R3 resistor

454 7.3.3 Switch Selection

The previous iteration of the pulser board utilised a BFR92 [7] high-speed RF NPN switching transistor which was directly driven by a LVDS-to-TTL converter. In the redesign phase, alternative circuit topologies were explored—particularly those suitable for generating (sub-)nanosecond pulses. This investigation led to the adoption of gate driver circuits. Gate drivers are advantageous not only because they can power switches with challenging drive requirements, but also because sub-nanosecond electrical pulses can be achieved by modulating the enable pin with slight timing offsets.

462 The fastest commercially available gate driver identified was the Texas Instruments  
 463 LMG1020 [8]. This device supports pulse widths down to 1 ns, with typical rise and fall  
 464 times of 400 ps. Additionally, it features an enable pin that allows for precise nanosecond  
 465 pulse shaping<sup>2</sup>. The LMG1020 is compatible with both Gallium Nitride Field Effect Tran-  
 466 sistor (GaN) and Metal Oxide Semiconductor Field Effect Transistor (MOSFET) switches,  
 467 broadening the scope for future component integration and experimentation. It is widely  
 468 available and priced at £1.97 per unit in the quantities we will require for full production.

469 For the switching element, enhancement-mode GaN transistors manufactured by EPC  
 470 were selected due to their superior switching characteristics. This recommendation origi-  
 471 nated from Nick Braam, an engineer at the University of Victoria, who contributed to the  
 472 pulser board design for the mPMT system [9]. Two EPC devices were shortlisted: the  
 473 EPC2012 [10] and EPC8004 [11]. The EPC2012 offers a simpler footprint, which could re-  
 474 duce manufacturing defects. However, the EPC8004 features lower parasitic capacitance,  
 475 see Figure 25 for the EPC2012 values and Figure 26 for EPC8004 values, leading to better  
 476 high-speed performance.

477 To evaluate optical output performance, a 40 m length of FP400URT [2] optical fibre,  
 478 a Mouser-sourced 385 nm LED (ATS2012UV385 [12]), and a Hamamatsu H10721-210 [13]  
 479 PMT were used. The EPC-based configurations exhibited nearly identical pulse shapes,  
 480 whereas the BFR92-based circuit's pulse shape was less sharp at identical pulse widths, as  
 481 shown in Figure 27. Consequently, the EPC8004 (Figure 28) was chosen for implementation.  
 482 Optimal performance of the EPC GaN switches required careful layout considerations. A  
 483 layout was developed in accordance with EPC's design guidelines [14], targeting minimal  
 484 parasitic inductance and capacitance. The design employs two layers placed directly above  
 485 one another, utilising large copper planes and multiple vias to ensure uniform current dis-  
 486 tribution. The PCB will be fabricated and assembled by PCB Train, using their 0.8 mm  
 487 thick, four-layer stack-up, which offers minimal inter-layer separation for optimal electrical  
 488 performance (Figure 19). This same layout strategy was applied to the BFR92 circuit to  
 489 provide a fair performance comparison.

490 A significant challenge at low pulse widths is the presence of a trailing edge or “tail” in  
 491 the LED output. This effect arises due to charge accumulation and the intrinsic capacitance  
 492 of the LED, resulting in extended decay times and pulse broadening (see Figure 29). To  
 493 mitigate this, a parallel modified snubber circuit was implemented, consisting of a 6.8 nH  
 494 inductor and a 3.3 Ω current-limiting resistor. Upon LED turn-off, the inductor generates an  
 495 electromotive force (EMF) that actively extracts residual charge from the LED, accelerating  
 496 its shutdown. The effectiveness of this approach is illustrated in Figure 30. Additionally,  
 497 two 0508 reverse-topology 100 nF capacitors have been incorporated. Their role is to act as  
 498 local energy reservoirs, providing rapid current delivery to the LED during pulse operation,  
 499 surpassing the response time of the main power supply.

eGaN® FET DATASHEET		EPC2012			
PARAMETER	TEST CONDITIONS	MIN	TYP	MAX	UNIT
<b>Dynamic Characteristics</b> ( $T_j = 25^\circ\text{C}$ unless otherwise stated)					
$C_{IS}$	Input Capacitance	$V_{DS} = 100\text{ V}, V_{GS} = 0\text{ V}$		128	145
$C_{OSS}$	Output Capacitance			73	95
$C_{RSS}$	Reverse Transfer Capacitance			3.3	4.4
					pF

Figure 25: EPC2012 Capacitance Values IC

<sup>2</sup>See page 12 and 13 in [8].

Dynamic Characteristics <sup>#</sup> ( $T_j = 25^\circ\text{C}$ unless otherwise stated)							
PARAMETER		TEST CONDITIONS		MIN	TYP	MAX	UNIT
$C_{ISS}$	Input Capacitance	$V_{GS} = 0\text{ V}, V_{DS} = 20\text{ V}$		45	52		pF
$C_{OSS}$	Output Capacitance			23	34		
$C_{RSS}$	Reverse Transfer Capacitance			0.8	1.3		

Figure 26: EPC8004 Capacitance Values IC

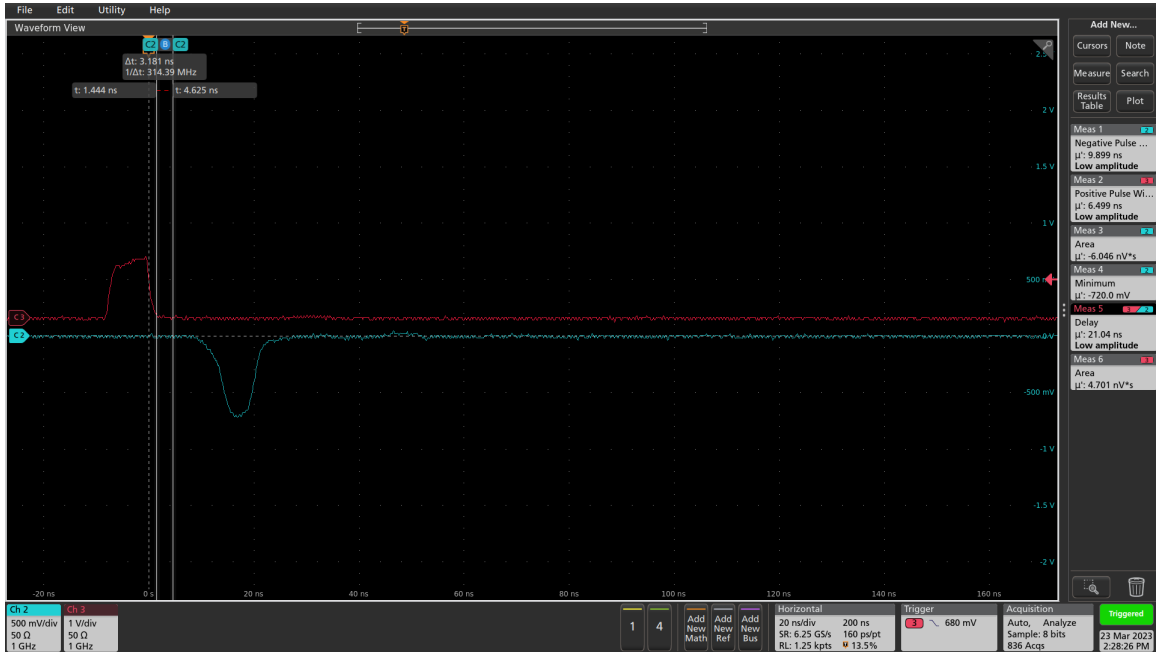


Figure 27: BFR92 Pulse Shape

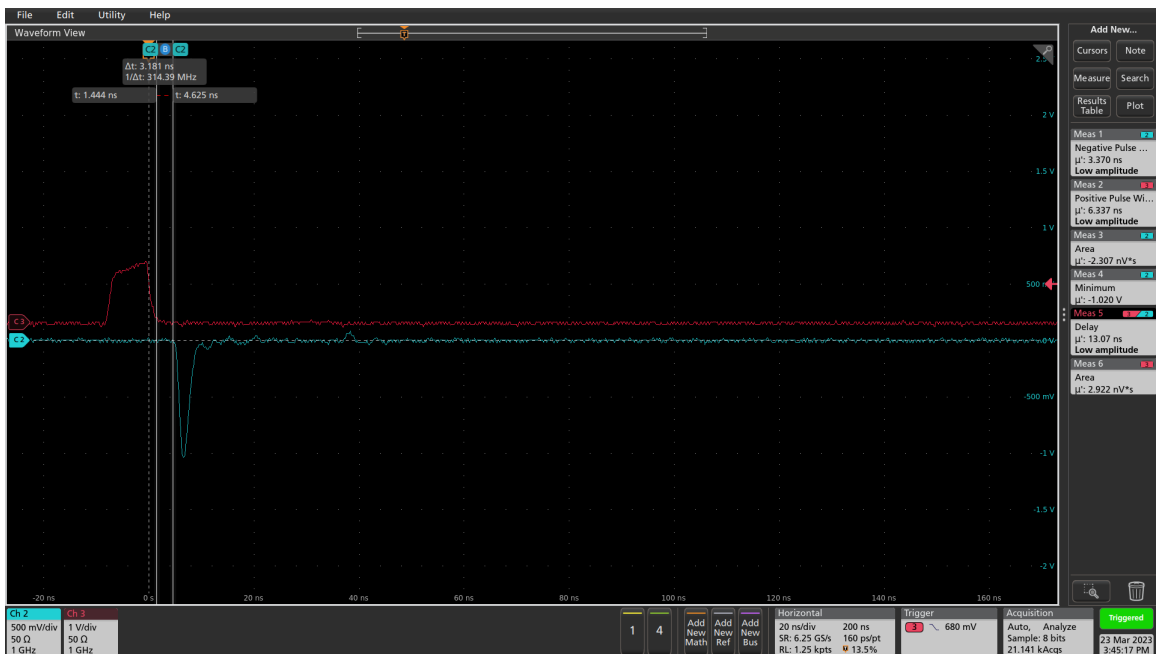


Figure 28: EPC8004 Pulse Shape

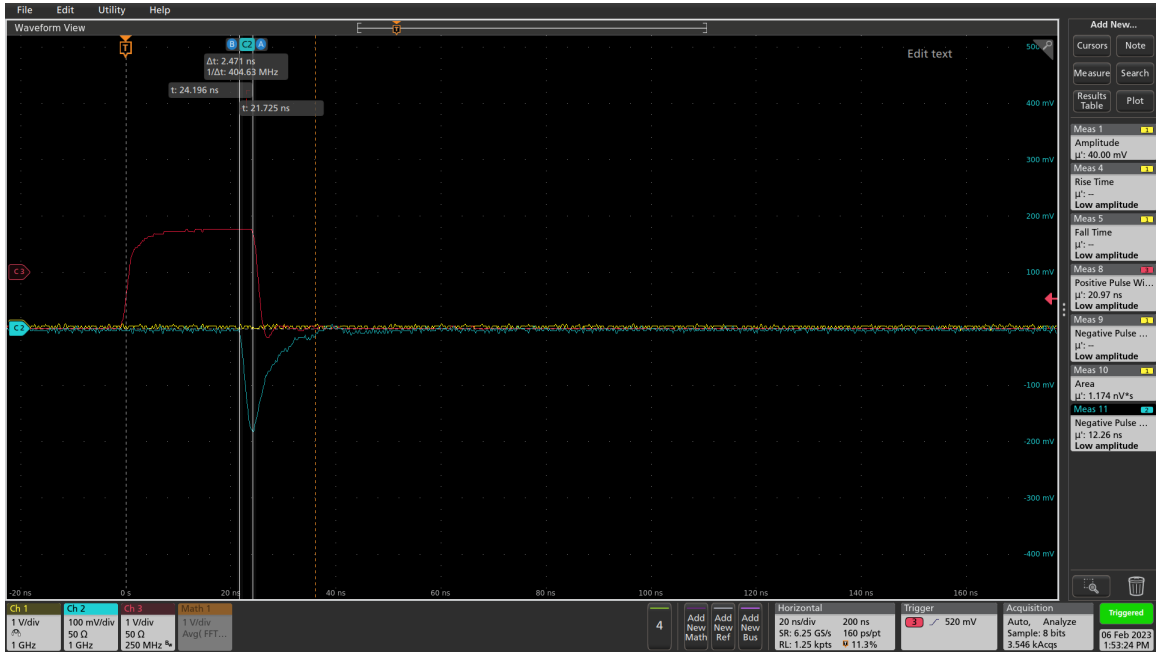


Figure 29: Pulsing Circuit With No Inductor and Resistor

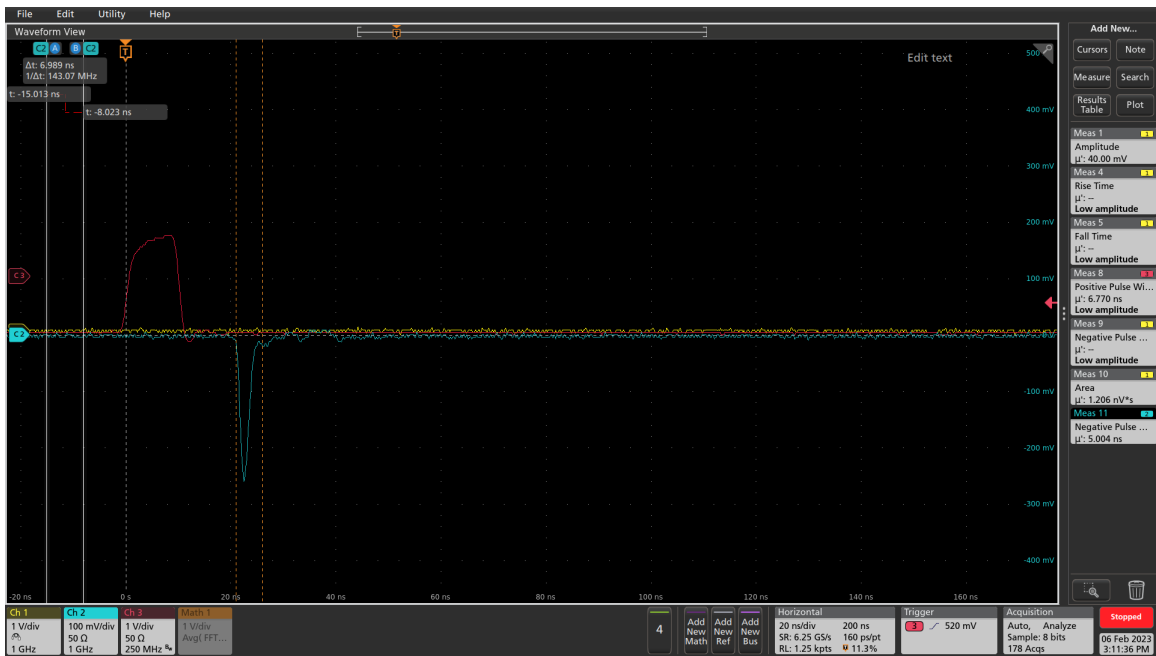


Figure 30: Pulsing Circuit With Inductor and Resistor

### 500 7.3.4 Testing

501 For testing purposes, the previous-generation United Kingdom Light Injection (UKLI) moth-  
 502 erboard and associated software were utilised in conjunction with a prototype of the next-  
 503 generation pulser board. This prototype consisted of four distinct circuit variants: one  
 504 employing the EPC8004 switch, another utilising the EPC2012 switch, a third using the  
 505 same high-speed transistor (BFR92) as implemented in the legacy system, and a fourth vari-  
 506 ant incorporating an EPC2012 gate in a through-hole package instead of the standard 0805  
 507 surface-mount footprint. Further evaluation was also performed using the latest pulser board  
 508 prototype once they had arrived.

509 Following comparative performance evaluations, the configuration using the EPC8004  
 510 switch was selected for continued use. While both the EPC8004 and EPC2012 switches  
 511 exhibited similar electrical characteristics, the EPC8004 offered superior performance due to  
 512 its lower parasitic capacitance, without any additional cost. The pulser board assembly was  
 513 housed within a dark box during testing, and a 3D-printed fibre coupler was employed to  
 514 facilitate light delivery. The initial focus of the evaluation was on the shape of the generated  
 515 optical pulse. During component selection, it was observed that the LED previously sourced  
 516 from Mouser (ATS2012UV385 by Kingbright) provided acceptable performance in terms of  
 517 electrical characteristics, but the optical output was suboptimal, as it was showing a strange  
 518 “double pulsing”, which can be seen in Figure 31. Additionally, this LED was found to be  
 519 out of stock and obsolete at the time after testing, precluding further procurement.

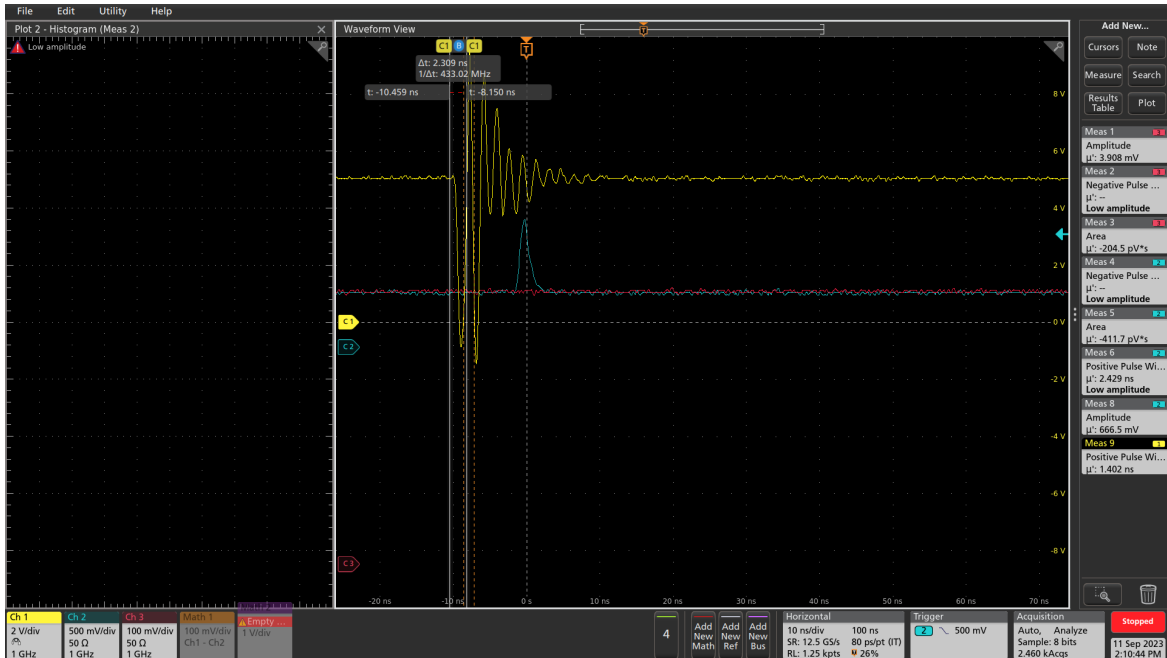


Figure 31: Double pulse observed from the Kingbright ATS2012UV385 LED.

520 Subsequently, four ultraviolet LEDs from LC LED were assessed—two emitting at 365 nm  
 521 and two at 395 nm—each in both 0805 and 0603 surface-mount packages. Results demon-  
 522 strated that the 0805 package LEDs provided significantly better optical coupling efficiency  
 523 with the FP400URT optical fibre. Furthermore, the 365 nm variant exhibited superior opti-  
 524 cal power output relative to the 395 nm counterparts. Based on these findings, the LC LED  
 525 UT-67UV365P [15] 365 nm LED was selected as the most suitable LED for this application.  
 526 Tests showed the LED was behaved well, providing an optical pulse of 2.8 ns width, with  
 527 3.3 ns eletrical signal, as shown as Figure 32. The pulse width deviation is 60.218 ps, or

528 2.12% , and the histogram shows the pulse distribution.

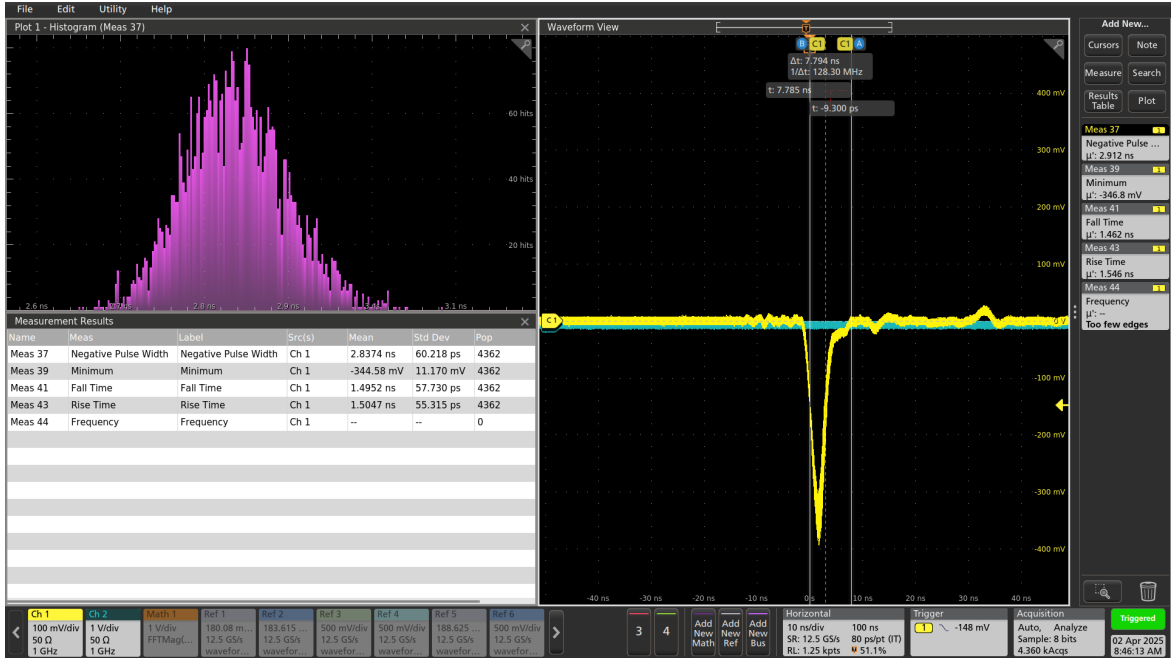


Figure 32: Scope trace and pulse width histogram for a 3.3 ns input signal, through a 1 m FP400URT fibre.

529 A long-term stress test was also performed for this LED. The pulser system was placed  
 530 in a small dark box, and a new 365 nm LED was soldered onto the pulser board. The pulse  
 531 frequency was set to 30,000 Hz, and the pulse width was set to 2.8 ns pulse width, which  
 532 yielded a 6.8 ns pulse after dispersion through 180 m of fibre. The system was running  
 533 continuously for 13 days, during which power and air temperature measurements were made  
 534 every 10 seconds. The air temperature was measured at the power meter, using the Thorlabs  
 535 PM100USB. Each individual LED is expected to run at around 0.0082 Hz, as the auto-calib  
 536 process is expected to pulse any channel at 1 Hz rate and there are 122 active channels. This  
 537 means that pulsing the LED at 30 KHz for 13 days is equivalent to 106,849 years of normal  
 538 running, not including the short dedicated calibration runs where the system will run at  
 539 1 kHz. While we have not calibrated the temperature gain, we are estimating a 1.5% loss if  
 540 we compare the same temperature from the beginning of the experiment to the end. **ADD**  
 541 **PLOT FOR THIS**

## 542 7.4 LVDS to TTL Converter

543 The DS90C402 [16] from Texas Instruments was selected as the LVDS-to-TTL conversion  
 544 solution. This device is a dual-channel converter, chosen primarily for its fast switching  
 545 characteristics—offering both rise and fall times of approximately 500 ps. It operates at  
 546 5 V and provides 5 V TTL output levels, which aligns well with the requirements of the  
 547 downstream switching circuitry. The inclusion of two channels is particularly advantageous,  
 548 as it enables the generation of sub-nanosecond differential pulses by precisely offsetting the  
 549 channels, as described in Switch Selection. Among commercially available devices with  
 550 these specifications, the DS90C402 is the fastest and is readily available through multiple  
 551 distributors.

552 The associated circuit was implemented in accordance with the manufacturer's recom-  
 553 mendations provided in the datasheet. A decoupling capacitor was placed in close proximity

554 to the power supply pin to minimise voltage ripple. Output traces were routed using polygon  
 555 fills to reduce impedance and enhance signal integrity, and a continuous ground plane was  
 556 placed beneath the signal layers to improve shielding and minimise electromagnetic interfer-  
 557 ence. The schematic for this is given in Figure 33.

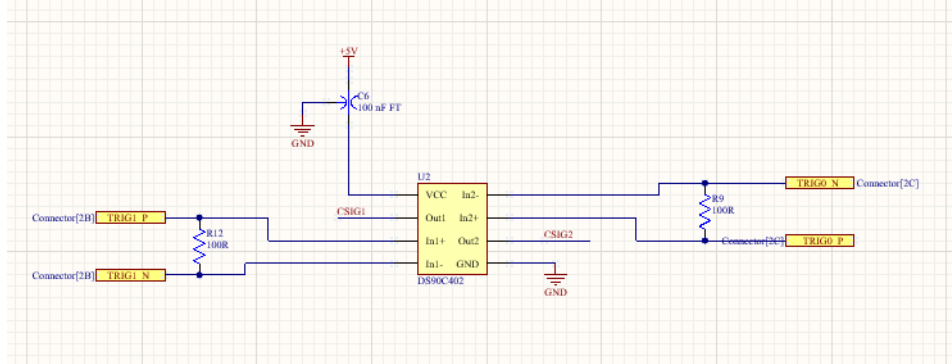


Figure 33: LVDS-TTL Converter Schematic

## 558 7.5 Power Supplies

559 Each pulser board is required to incorporate a variable voltage power supply dedicated  
 560 to driving the LED, with an adjustable output range from 3 V to 12 V. This supply is  
 561 used exclusively to modulate the LED’s light output by varying the forward voltage, and  
 562 consequently the current. The design specification also necessitates that the power supply  
 563 be remotely controllable—i.e., capable of being switched on or off via a simple logic-level  
 564 signal.

565 For this purpose, the LT1963A [17] adjustable low-dropout linear regulator was selected.  
 566 This regulator has demonstrated reliable performance in previous pulser board iterations  
 567 and offers a favourable balance of cost-effectiveness and controllability. The implementation  
 568 includes standard filtering and decoupling, with layout details provided in Figure 34. The  
 569 schematic provided in Figure 35 is an early version used for prototyping; the adjustable  
 570 circuit has been simulated and will be tested shortly, and the enable circuit has been tested,  
 571 modified and simplified. Updated schematics will be provided with v1.0 circuit. There will  
 572 be overcurrent protection built in to the system as well. A ZXCT1051 (Reference!) is used  
 573 to monitor the current and if it senses larger than normal current then it send a signal to  
 574 the FPGA to turn the damaged board off. A surface mounted fuse will be added in line as  
 575 well to make sure there is a second line of defense as well.

576 In addition to the variable LED supply, each board requires a stable 5 V supply to power  
 577 both the DS90C402 LVDS-to-TTL converter and the LMG1020 gate driver. Unlike the LED  
 578 supply, this rail remains continuously powered. The 5 V supply is provided by an LM2937-5  
 579 [18], a fixed-output linear voltage regulator, which has been successfully employed in various  
 580 high-speed and low-noise applications within the laboratory. The associated circuit schematic  
 581 and layout and schematic are shown in Figures 36 and 37 respectively.

582 To meet system-level design constraints, each pulser board is equipped with its own  
 583 independent 12 V input supply, ensuring that LED output intensity can be individually  
 584 controlled on a per-board basis. However, the 5 V supply is common across all boards  
 585 and derived locally on each pulser module. This approach allows for localised filtering and  
 586 minimal power distribution path lengths, reducing the risk of noise coupling and voltage  
 587 drop considerations that are particularly critical in high-speed circuit applications.

588 Power is supplied to each board via the Eurocard backplane. The 12 V input from the

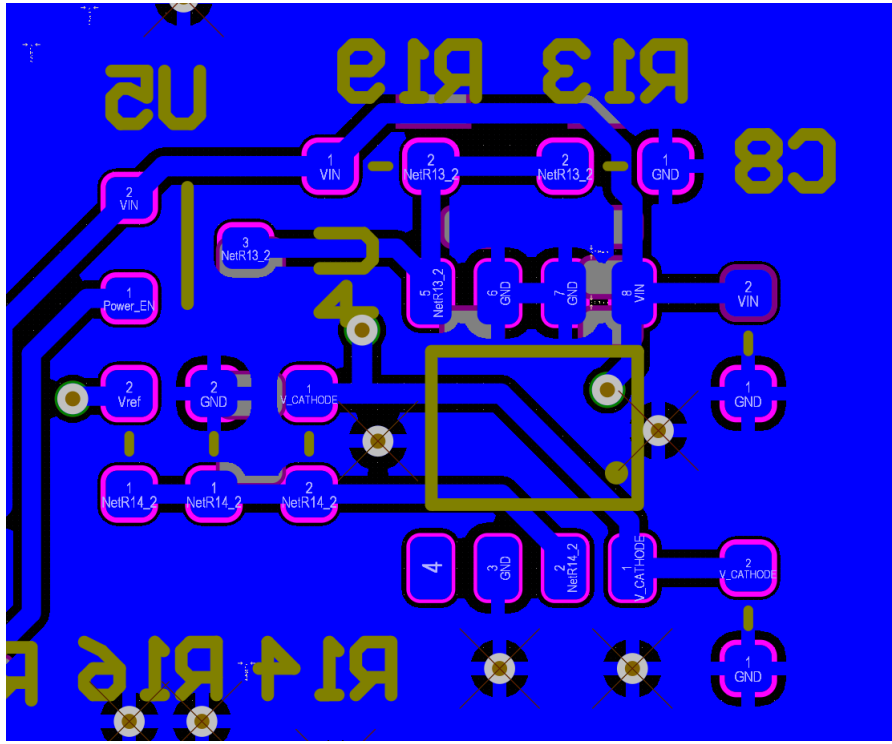


Figure 34: LT1963 Layout

589 Eurocard simultaneously feeds both the variable (LED) and fixed (logic) power regulators  
 590 on the pulser board. The LED enable function is controlled via a 5 V logic signal originating  
 591 from the Eurocard’s GPIO interface. Additionally, a DAC output from the Eurocard provides  
 592 a voltage control signal to the adjustment pin of the LT1963A regulator on each pulser board,  
 593 thereby allowing precise, programmable control of light intensity.

## 594 7.6 Connector

595 The previous board connector was deemed too bulky and expensive for the larger number  
 596 of channels needed in this system, leading to the process of finding a more suitable alterna-  
 597 tive. Following an evaluation of commercially available options, the Phoenix Contact female  
 598 connector 1331962 [19] was selected. This connector offers several advantageous specifica-  
 599 tions: it is rated for 500 V, features a low contact resistance of  $40\text{ m}\Omega$ , supports a maximum  
 600 current of 0.5 A, and is capable of signal transmission up to  $20\text{ Gbit s}^{-1}$ . In addition, it is  
 601 cost-effective, priced at approximately £0.50 per unit, with wide availability ensuring ease  
 602 of procurement. Multiple height variants are available within the same series, facilitating  
 603 flexible mechanical integration within the Eurocard crate system. The compact footprint of  
 604 the connector allows for a reduced PCB form factor. Electrically, the high-frequency perfor-  
 605 mance supports reliable LVDS signal transmission. Additionally, the compact footprint of  
 606 the connector is well-suited to space-constrained PCB layouts.

607 An illustration showing the connector and corresponding circuit layout is provided in  
 608 Figure 38.

## 609 7.7 Fibre Coupler

610 During the prototyping phase, improvements were made to the PCB layout to better ac-  
 611 commodate a fibre coupler. As a result, the current design includes provisions for precise

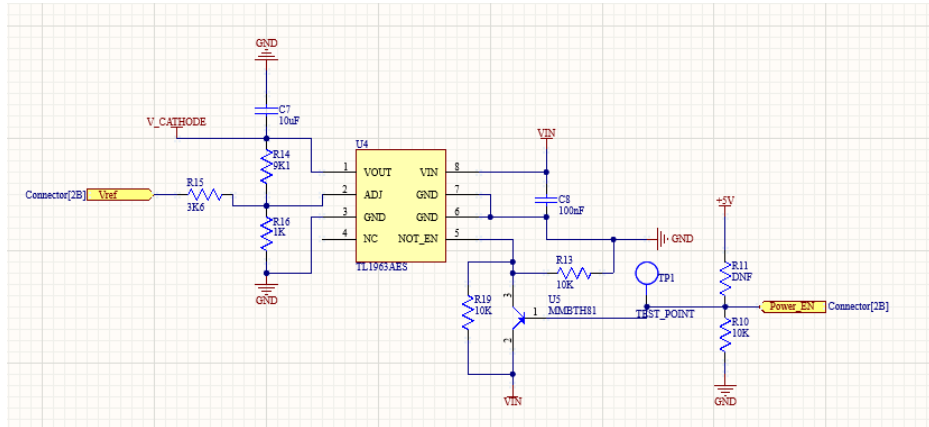


Figure 35: 12V Circuit Schematics

mechanical mounting and alignment. Specifically, two mounting holes for M2 screws have been incorporated, enabling the 3D-printed coupler to be firmly secured to the board (see Figure 39). In addition, two dowel holes have been added to guide the coupler into position, ensuring accurate alignment over the LED. Given the tolerances associated with PCB fabrication and 3D printing, an alignment accuracy of approximately 100  $\mu\text{m}$  is expected.

To optimise the electrical path, capacitors have been repositioned as close as possible to the LEDs. This minimises parasitic inductance and resistance, while enabling a centralised layout of larger components. The resulting configuration creates a compact chamber housing both the LEDs and associated capacitors.

The design for the fibre coupler is modular, consisting of three components: a base section mounted to the pulser PCB, a top section into which the fibres will be epoxied, and an intermediate attenuator element. The latter part will be added to the current design to space the fibre from the LED and thereby adjust the optical coupling efficiency to achieve required attenuation, accounting for the different lengths of fibre in the system. This means the attenuation will be implemented within the coupler itself, allowing the LED output to remain within the electronically controlled dynamic range.

The fibre coupler will be fabricated via stereolithography (SLA) using a black resin to minimise light transmission through the material. Additional light-tight testing will be conducted, and black paint may be applied if further sealing is required. Furthermore, laser-cut rubber gaskets will be introduced at interface points to ensure optimal optical isolation and mechanical sealing.

## 7.8 Photon Yield Tests

tests on maximising photon yield and available dynamic range should be fully described here

## 7.9 Production

Production will be carried out using PCB Train as they are local and competitively priced, and known to produce boards of good quality. Estimated cost is £12.27 per board, which equates to £1,496.94 for 122 units or £1,840.5 for 150 units, and production is £4073.48 for 122 units for 15 days lead time, or £3985 for 150 units at 25 days lead time. The full cost breakdown is shown in Figure 40

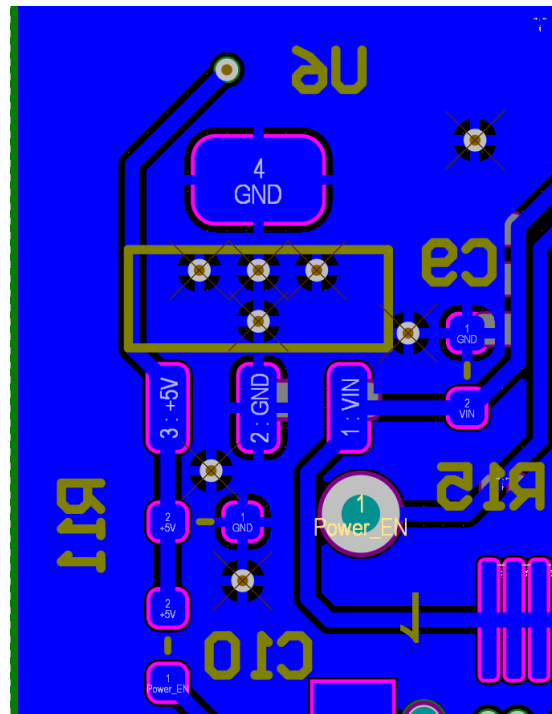


Figure 36: LM2937-5 Layout

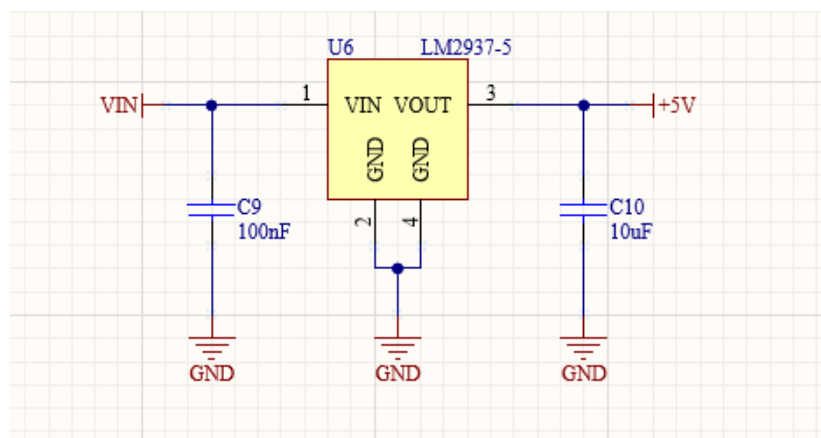


Figure 37: 5V circuit schematics

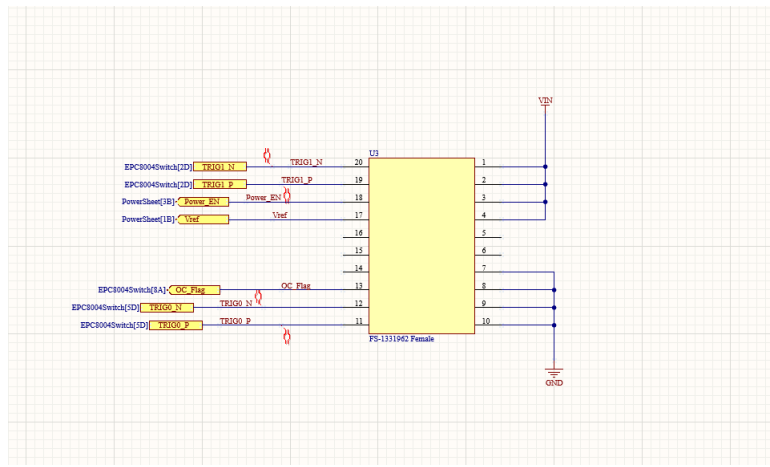


Figure 38: Connector Schematics



Figure 39: Fibre Coupler Design

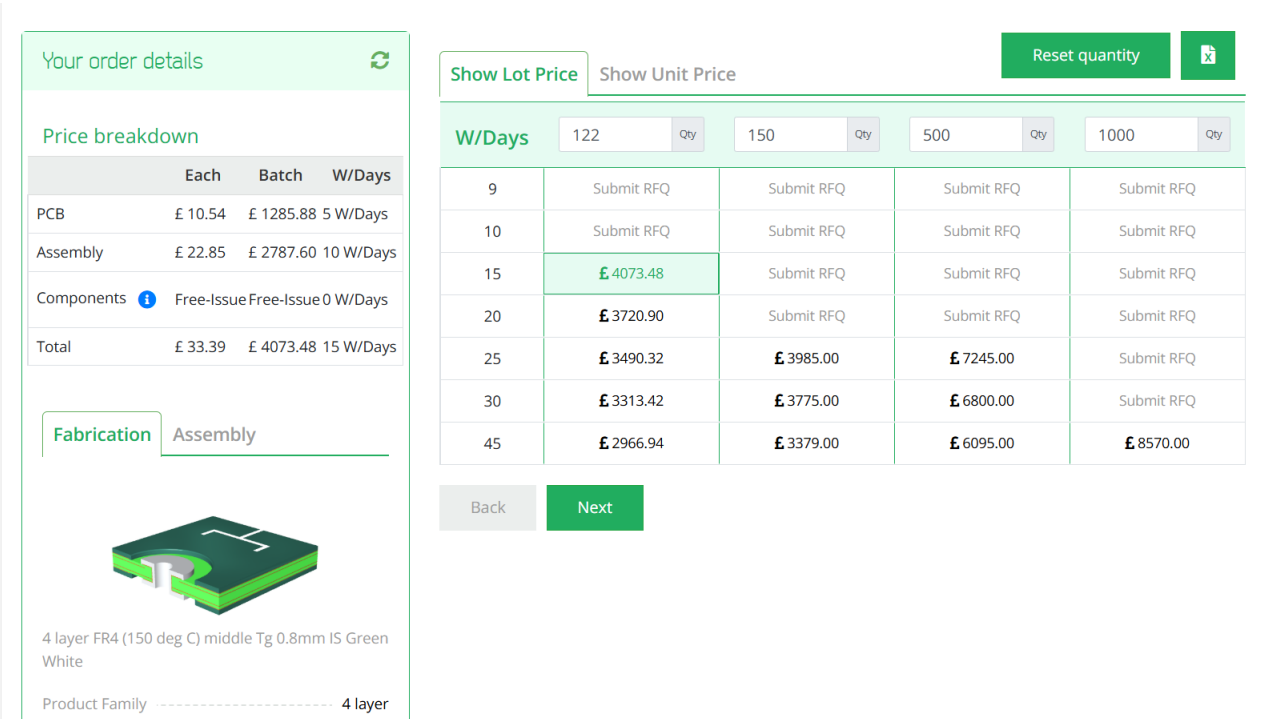


Figure 40: PCBTrain PCB production and assembly costs

## 641 7.10 Changes Expected from v0.9 to v1.0

### 642 7.10.1 LED and Switching Circuit

643 There will be minimal changes to the LED and switching circuit. Changes will be made to  
 644 the position of the switching devices, placing them slightly closer to each other to reduce  
 645 transmission line length. The LED will likely remain as the LC LED UT-67UV365P 365nm  
 646 0805 LED, but further LED tests will be performed. This takes a short amount of time, and  
 647 may lead to discovering better LEDs in the future which would be easy to swap in due to  
 648 standardised footprints.

### 649 7.10.2 LVDS-to-TTL Converter

650 No changes are expected to this circuit.

### 651 7.10.3 Power Supplies

652 Reverse voltage bias will be removed as no difference between normal and reverse bias was  
 653 observed photon output. The overcurrent protection and power enable circuit will be re-  
 654 worked.

### 655 7.10.4 Connector

656 No changes are expected to this.

### 657 7.10.5 Fibre Coupler

658 A brand new fibre coupler will be designed due to the recent requirement changes regarding  
 659 the different fibre lengths.

660 **8 Server Rack and Cooling**

661 To house the electronics for the LI systems, two 42U server racks with 800 mm depth will  
662 be used. The front of the server rack will be used for electrical connections and displays,  
663 and the reverse/internal will be used only for fibre routing. The server racks will include  
664 Uninterruptible Power Supplies (UPS) for safe power delivery and for power processing, to  
665 avoid issues with potential instabilities in the main power supply. Each rack will include an  
666 air conditioning unit to have a controlled temperature and remove humidity from the air,  
667 as the relative humidity in the air is expected to be above 70%. Although specific tests on  
668 running the LED electronics in humid conditions have not been carried out, it is known that  
669 the optical switches for the laser calibration system requires lower humidity levels. In order  
670 to simplify things and remove the potential of humidity issues with the LED electronics,  
671 both server racks will be air conditioned. These systems are widely available and will be  
672 chosen closer to installation.

673 **9 LED Monitoring**

674 To monitor the light output from the LEDs before attenuation by fibres and convolution  
675 with water parameters, PMTs will be placed near to the LED sources. This is a similar  
676 design to what is currently used in the Super-K UKLI system. Each LED connector will  
677 feature a second fibre to take light to a series of PMTs, which are expected to be Hamamatsu  
678 H10721-210. Due to the 8 mm diameter of the PMT window, up to 16 fibres can be attached,  
679 meaning one PMT can monitor up to 16 LED boards at once. Each PMT will be powered  
680 by a unique low cost power supply developed for the SK UKLI system. These will be housed  
681 in a small 2–3 U server rack. The signals from the PMTs will then go to the dedicated HK  
682 electronics channels that are set up for monitoring.

683 **10 Control System for LEDs**

684 The LEDs are driven by a differential LVDS signal originating from the FPGA. The FPGA  
685 in use is the Genesys 2 [20] development board, which operates a pulsing VHDL module  
686 clocked at 300 MHz. Pulses are generated on the rising edge of this clock, and toggling the  
687 output (i.e., asserting and then deasserting the trigger) requires a minimum of two clock  
688 cycles. Consequently, the shortest achievable pulse duration in this configuration is 3.3 ns.

689 One of the main limitations of this setup is the coarse time resolution: pulse durations  
690 are effectively constrained to integer multiples of 3.3 ns. To achieve a broader and more  
691 finely resolved spectrum of optical injection into the detector, improved temporal precision  
692 is necessary. This is accomplished using the Xilinx IODELAY primitive, originally designed for  
693 high-speed interface timing alignment. The IODELAY module permits fine-tuning of signal  
694 timing to account for PCB trace mismatches, and in this application, it is repurposed to  
695 introduce controlled delays between pulses.

696 To generate shorter pulses, two identical signals are created, one of which is delayed  
697 using IODELAY. These signals are then combined using a logical AND operation, producing  
698 a narrower pulse. Since the IODELAY module requires one clock cycle to process the input,  
699 both signals—regardless of whether they are delayed—must pass through an IODELAY stage  
700 to ensure temporal synchronisation.

701 Conversely, to produce longer pulses, the same methodology is applied, but the signals are  
702 combined using a logical OR gate instead. This approach extends the pulse width beyond the  
703 base clock resolution, enabling pulse durations ranging from approximately 1.5 ns to 4.5 ns

704 in 49 discrete steps. The lower bound is determined by the threshold of the LVDS-to-TTL  
705 converter, which does not respond to pulses shorter than approximately 1.5 ns .

706 For channels using the longest optical fibres, this extended range is sufficient, given  
707 the intrinsic dispersion in the fibre optics of around 5 ns. However, shorter fibres require  
708 additional pulse shaping. To this end, an additional mechanism is implemented using a `for`  
709 loop structure within the FPGA logic. This allows the pulse to persist for multiple clock  
710 cycles, effectively producing longer pulses by repetition. However, due to FPGA architecture  
711 constraints, each iteration of the loop consumes a clock cycle, necessitating careful timing  
712 control. For instance, to produce a 6.6 ns pulse, the loop must be configured for two cycles,  
713 accounting for the loop overhead.

714 Further refinement is under investigation through the daisy-chaining of multiple `IODELAY`  
715 modules. This would enable sub-nanosecond granularity by introducing additional interme-  
716 diate delay steps. While promising, this technique requires further validation and testing.

717 The pulse control data structure is currently under development. There are two types  
718 of pulse description considered. In the first option, the software interface would require two  
719 parameters per channel: a *coarse* step and a *fine* step, reflecting the approach used in the SK  
720 system. The other option would be just a single variable and then simple logic turning that  
721 variable into the *coarse* and *fine* step that the internal logic requires. Two hardware modules  
722 are planned: one for generating the single shortest possible pulse (to minimise latency), and  
723 another for multi-cycle pulses using programmable duration. A selection logic will assess the  
724 input and route it to the appropriate module based on the desired pulse characteristics.

725 Each LED channel will be controlled independently, allowing for unique pulse configu-  
726 rations across channels. The global trigger will be derived from the system clock, and each  
727 channel will pulse in a predefined sequence while triggered from the global trigger. This  
728 architecture also supports simultaneous pulsing of multiple channels. Should asynchronous  
729 behaviour be required, additional per-channel delay logic can be implemented. Given the  
730 five distinct fibre lengths used in the system, each channel group will also include a config-  
731 urable delay offset to compensate for propagation time differences. These group delays will  
732 be calibrated and fixed, with the option of fine-tuning individual channels post-deployment  
733 if necessary.

734 The repetition rate can be adjusted as well, including a single pulse, using external  
735 trigger, from 0.001Hz through 1 KHz to multiple megahertz if needed, but the system was  
736 only tested up to 30 KHz, as that was a high enough rate to illuminate the power monitor's  
737 sensor.

738 The FPGA programming remains in active development. Inter-crate communication  
739 protocols and synchronisation are currently under integration and testing.

## 740 11 Crate Electronics

### 741 11.1 Overview

742 The system specification calls for control of up to 122 LED channels, significantly exceeding  
743 the channel counts used in current systems such as Super-Kamiokande or LUX-ZEPLIN,  
744 which the previous generation of pulser boards are used for. To manage this complexity, the  
745 design prioritises ease of use, maintainability, and straightforward deployment, particularly  
746 given that the server racks will accommodate hundreds of optical fibres.

747 To achieve this, a system concept originally developed by ATLAS collaborators (specifi-  
748 cally by Ashley Greenal) has been adapted. The original design utilises a Genesys 2 FPGA  
749 integrated into a half-width Verotec KM6-2 [21] Eurocard-compatible crate for testing pur-  
750 poses. This concept has been extended to a full 19-inch rack width, enabling the integration

751 of up to 36 pulser boards within a single crate.

752 Each FPGA is capable of interfacing with up to 38 pulser boards, thereby maximising  
753 the utilisation of available LVDS differential pairs, with an additional pair reserved for the  
754 laser trigger signal. This configuration ensures full use of the Genesys 2's I/O capacity while  
755 maintaining flexibility for future expansion.

756 The system architecture consists of three primary components: the Blade (Section 11.2),  
757 Backplane (Section 11.3) and Eurocard (Section 11.4). This modular approach ensures  
758 scalability and facilitates debugging, replacement, and upgrades. It also provides a robust  
759 foundation for managing high channel counts while maintaining signal integrity and synchro-  
760 nisation across the system.

761 The system will consist of four crates, which allows for up to 144 pulser boards. The  
762 OD diffuser system required 122 boards to run, and the auto-Xenon calibration system is  
763 expected to use one or two of the additional boards. This means there will be 20 spare boards  
764 available for hot-swapping. These can be further grouped into five sets of four, to have four  
765 spare boards for each of the five different fibre lengths. Should issues arise, a local technician  
766 can remove the signal and monitor fibres from the broken pulser board, attach them to a  
767 spare board, and reconfigure the software to use the spare board for running, all with remote  
768 expert guidance. Next time an expert is on site they can do further maintenance or repair  
769 if needed.

## 770 11.2 Blade

771 The Blade is a simple, eight layer board, that has a SEAM-40-06.5-L-10-2-A-K-TR [22]  
772 connector which is a direct fit for the Genesys 2's FMC connector. It features a PCIE 16X  
773 connector at the edge for connectivity to the Backplane. The PCIE was selected by Ashley  
774 Greenal as it is a well documented standard connector and there are a large amount of  
775 connectors available that can be bought easily. While PCIE connectors are being used, the  
776 PCIE standards for communication are not. This is a very dense PCB with all the differential  
777 tracks on it, so buried vias and multiple layers will be used. See Figure 41 for a work in  
778 progress version.

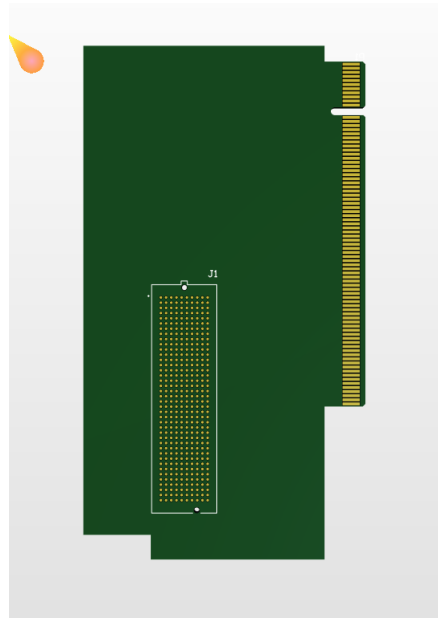


Figure 41: Blade Work in Progress

### 779 11.3 Backplane

780 The Backplane serves two primary functions: the distribution of differential signals from the  
781 Blade to the Eurocards, and the reception and distribution of power throughout the crate  
782 system. It accepts external power inputs of 12 V and  $\pm 5$  V, and includes a basic regulation  
783 circuit to stabilise these supply voltages for downstream use.

784 Given the mechanical constraints and routing complexity, the Backplane is implemented  
785 as a four-layer PCB with impedance-controlled traces to ensure signal integrity across all  
786 differential pairs. It features a single PCIe x16 connector to interface with the Blade, and  
787 three PCIe x8 connectors to interface with the Eurocards.

788 The Eurocards are positioned at slots 2, 8, and 64 within the crate. This arrangement  
789 creates two symmetrical chambers with 48 units spacing between cards, ensuring adequate  
790 space to accommodate the minimum long-term bend radius of the FP400URT optical fibres.  
791 This layout balances mechanical reliability with signal routing efficiency and supports long-  
792 term maintainability of the system. See Figure 42 for a work in progress version.

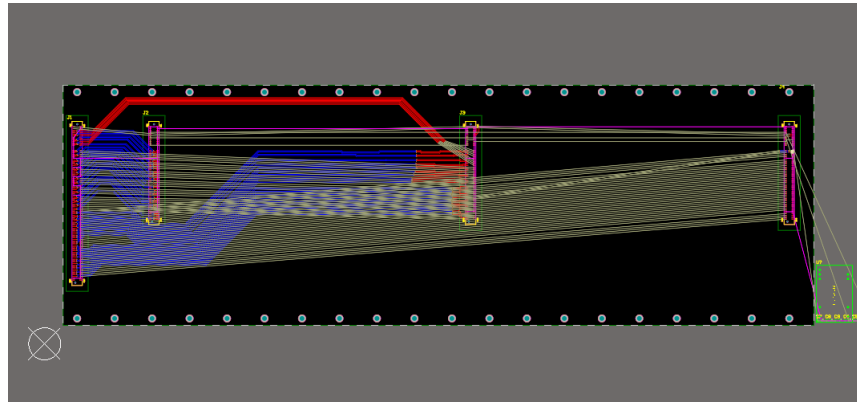


Figure 42: Backplane Work in Progress

### 793 11.4 Eurocard

794 The Eurocard format defines the physical and electrical standard for the crate system, hence  
795 the naming convention. Each Eurocard is equipped with a PCIe x8 connector for interfacing  
796 with the Backplane, and is designed to host up to 18 pulser boards—nine mounted on each  
797 face. Pulser boards connect via FS-1332120 Male[23] connectors, and each socket includes  
798 two mounting holes for mechanical standoffs.

799 The board layout on each side consists of two staggered rows: five sockets in the back  
800 row and four in the front. The two faces are laterally offset by approximately 10 mm to  
801 prevent interference or fibre clashes when the system is fully populated and enclosed within  
802 the crate chamber. This offset ensures smooth fibre routing and accommodates the bend  
803 radius requirements of FP400URT fibres.

804 Power distribution within each Eurocard is handled by a THD 12-1212 [24]12 V DC-DC  
805 regulator. This regulator provides local power isolation for the pulser boards and includes  
806 a control pin connected to a PCA9698 [25] 40-pin GPIO expander. This allows for system-  
807 level control, enabling or disabling all pulser boards on a card—an essential feature during  
808 power-up, especially when the FPGA may inadvertently drive all differential outputs high  
809 during reprogramming.

810 The GPIO expander is responsible for enabling the local 12 V regulator and for selectively  
811 powering individual pulser boards. This facilitates fault isolation and power savings in

812 channels that are inactive or disconnected. Additional GPIO pins are assigned to monitor  
813 output voltage levels via the overcurrent sensing circuitry.

814 To provide per-channel LED power control, an AD5673 [26] DAC is included. It outputs  
815 analogue control voltages to the onboard adjustable regulators on each pulser board,  
816 allowing for independent LED drive voltage per channel. Both the GPIO and DAC devices  
817 communicate with the system over the I<sup>2</sup>C protocol.

818 For laser synchronisation, the Eurocard includes a differential-to-NIM conversion stage.  
819 This consists of an LVDS-to-TTL converter identical to that used on the pulser boards,  
820 followed by a TTL-to-NIM converter. This ensures compatibility with legacy NIM-based  
821 timing systems used in external laser triggering. See Figure 43 for a work in progress version.

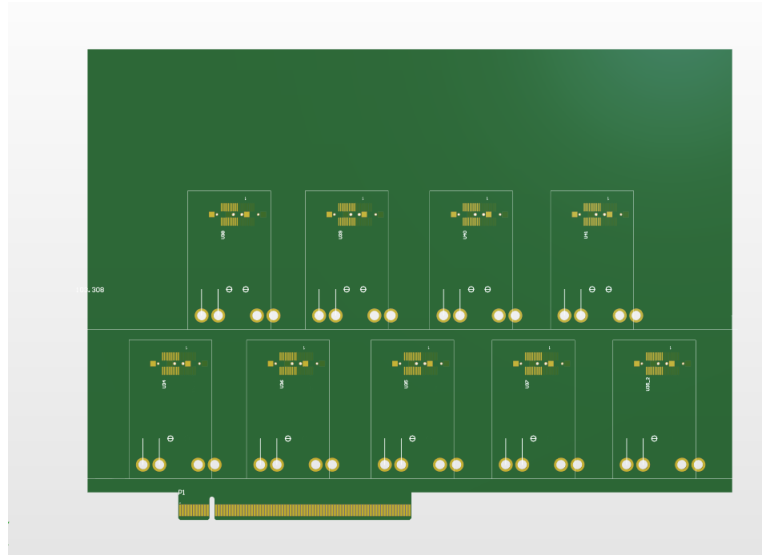


Figure 43: Eurocard Work in Progress

## 822 12 Conclusions

823 Write this

## 824 References

- 825 [1] S. Jenkins *et al.*, “HK LI Fibre Specifications,” HK-TN-0091, Aug. 2025.
- 826 [2] Thorlabs. “FP400URT Datasheet.” (2022), [Online]. Available: <https://www.thorlabs.com/drawings/7ade35b092fac3f3-EFB2F350-971A-B4B4-29D36C92039FB538/FP400URT-SpecSheet.pdf> (visited on 07/17/2025).
- 827 [3] Hyper-Kamiokande Outer Detector Group: D. Lodovico, E. Drakopoulou, G. Erofeev,  
828 *et al.*, “Outer detector technical report,” HK-TN-0064, 2022.
- 829 [4] H.-K. Collaboration. “WCSim Version 1.12.26.” (2018), [Online]. Available: <https://github.com/WCSim/WCSim/releases/tag/v1.12.26> (visited on 09/16/2025).
- 830 [5] S. Boyd *et al.*, “Hyper-Kamiokande light injector diffuser technical note,” HK-TN-0042,  
831 May 2023.
- 832 [6] N. E. M. Association. “NEMA STANDARDS PUBLICATION NO. LI 1-1998.” (1998),  
833 [Online]. Available: <https://www.nema.org/docs/default-source/standards-document-library/li1.pdf> (visited on 08/19/2025).

- 838 [7] I. T. AG. “BFR 92P E6327 Datasheet.” (2009), [Online]. Available: [https://www.mouser.co.uk/datasheet/2/196/Infineon\\_LNA\\_BFR92P\\_14-73949.pdf](https://www.mouser.co.uk/datasheet/2/196/Infineon_LNA_BFR92P_14-73949.pdf) (visited on 07/17/2025).
- 841 [8] T. I. Incorporated. “LMG1020 Datasheet.” (2018), [Online]. Available: [https://www.ti.com/lit/ds/symlink/lmg1020.pdf?ts=1752716909774&ref\\_url=https%253A%252F%252Fwww.mouser.cn%252F](https://www.ti.com/lit/ds/symlink/lmg1020.pdf?ts=1752716909774&ref_url=https%253A%252F%252Fwww.mouser.cn%252F) (visited on 07/17/2025).
- 844 [9] N. Braam *et al.*, “LED-mPMTs for hyperK,” HK-TN-0052, Oct. 2023.
- 845 [10] E. P. C. Corporation. “EPC2012 Datasheet.” (2012), [Online]. Available: [https://epc-co.com/epc/Portals/0/epc/documents/datasheets/EPC2012\\_datasheet.pdf](https://epc-co.com/epc/Portals/0/epc/documents/datasheets/EPC2012_datasheet.pdf) (visited on 07/17/2025).
- 848 [11] E. P. C. Corporation. “EPC8004 Datasheet.” (2023), [Online]. Available: [https://epc-co.com/epc/Portals/0/epc/documents/datasheets/EPC8004\\_datasheet.pdf](https://epc-co.com/epc/Portals/0/epc/documents/datasheets/EPC8004_datasheet.pdf) (visited on 07/17/2025).
- 851 [12] Kingbright. “ATS2012UV385 Datasheet.” (2021), [Online]. Available: <https://www.mouser.co.uk/datasheet/2/216/ATS2012UV385-1374632.pdf> (visited on 07/17/2025).
- 853 [13] H. P. K.K. “H10721-210 Datasheet.” (2024), [Online]. Available: [https://www.hamamatsu.com/content/dam/hamamatsu-photonics/sites/documents/99\\_SALES\\_LIBRARY/etd/H10720\\_H10721 TPM01062E.pdf](https://www.hamamatsu.com/content/dam/hamamatsu-photonics/sites/documents/99_SALES_LIBRARY/etd/H10720_H10721 TPM01062E.pdf) (visited on 07/17/2025).
- 856 [14] E. P. C. Corporation. “Design of High Current Nanosecond Resonant Pulse Drivers for Laser Diodes, Lidar, and other Applications.” (2025), [Online]. Available: <https://epc-co.com/epc/Portals/0/epc/documents/application-notes/AN032%20Design%20of%20High%20Current%20Nanosecond%20Resonant%20Pulse%20Drivers.pdf> (visited on 07/17/2025).
- 861 [15] L. LED. “ut-67uv365p Datasheet.” (2018), [Online]. Available: <https://www.lc-led.com/products/ut-67uv365p.html> (visited on 08/21/2025).
- 863 [16] T. I. Incorporated. “DS90C402 Datasheet.” (2013), [Online]. Available: <https://www.ti.com/lit/ds/symlink/ds90c402.pdf> (visited on 07/17/2025).
- 865 [17] A. Devices. “LT1963 Datasheet.” (2021), [Online]. Available: <https://www.mouser.co.uk/datasheet/2/609/lt1963a-2256452.pdf> (visited on 07/17/2025).
- 867 [18] T. I. Incorporated. “LM2347-5 Datasheet.” (2014), [Online]. Available: <https://www.ti.com/lit/ds/symlink/lm2937.pdf> (visited on 07/17/2025).
- 869 [19] P. Contact. “1331962 Datasheet.” (2025), [Online]. Available: <https://www.phoenixcontact.com/en-us/products/smd-female-connectors-fs-0635-20-fv-r-40-1331962?type=pdf> (visited on 07/17/2025).
- 872 [20] Digilent. “Genesys 2 Datasheet.” (2017), [Online]. Available: [https://digilent.com/reference/\\_media/reference/programmable-logic/genesys-2/genesys\\_2\\_rm.pdf?srsltid=AfmBOorhD9699F1FTC059o719HmCW-0XnEORnRJf6Thzcvu0vMs-pbAf](https://digilent.com/reference/_media/reference/programmable-logic/genesys-2/genesys_2_rm.pdf?srsltid=AfmBOorhD9699F1FTC059o719HmCW-0XnEORnRJf6Thzcvu0vMs-pbAf) (visited on 07/17/2025).
- 876 [21] Verotec. “Verotec KM6-2 Datasheet.” (2017), [Online]. Available: <https://www.verotec.co.uk/tech-downloads/Section%201%20-%20KM6-II%20Subracks.pdf> (visited on 07/17/2025).
- 879 [22] Samtec. “SEAM-40-06.5-L-10-2-A-K-TR Datasheet.” (2025), [Online]. Available: [https://suddendocs.samtec.com/catalog\\_english/seam.pdf?\\_gl=1\\*1soskal\\*\\_gcl\\_au\\*0DQw0DM2MjE4LjE3NTI3NDg2NTY.\\*\\_ga\\*MTAxNjAx0TQwNS4xNzUyNzQ4NjU2\\*\\_ga\\_3KFNZC07WW\\*cxE3NTI3NDg2NTUkbzEkZzAkDE3NTI3NDg2NTUkajYwJGwwJGgw](https://suddendocs.samtec.com/catalog_english/seam.pdf?_gl=1*1soskal*_gcl_au*0DQw0DM2MjE4LjE3NTI3NDg2NTY.*_ga*MTAxNjAx0TQwNS4xNzUyNzQ4NjU2*_ga_3KFNZC07WW*cxE3NTI3NDg2NTUkbzEkZzAkDE3NTI3NDg2NTUkajYwJGwwJGgw) (visited on 07/17/2025).

- 884 [23] P. Contact. "1332120 Datasheet." (2025), [Online]. Available: <https://www.phoenixcontact.com/en-us/products/smd-male-connectors-fs-0635-20-mv-r-50-1332120?type=pdf> (visited on 08/21/2025).
- 885
- 886
- 887 [24] T. E. AG. "THD 12-1212 Datasheet." (2025), [Online]. Available: [https://www.tracopower.com/sites/default/files/products/datasheets/thd12\\_datasheet.pdf?t=1752706801](https://www.tracopower.com/sites/default/files/products/datasheets/thd12_datasheet.pdf?t=1752706801) (visited on 07/17/2025).
- 888
- 889
- 890 [25] N. B.V. "PCA9698 Datasheet." (2010), [Online]. Available: <https://www.nxp.com/docs/en/data-sheet/PCA9698.pdf> (visited on 07/17/2025).
- 891
- 892 [26] A. Devices. "AD5673 Datasheet." (2020), [Online]. Available: <https://www.analog.com/media/en/technical-documentation/data-sheets/ad5673r-5677r.pdf> (visited on 07/17/2025).
- 893
- 894